THE ASTROPHYSICAL JOURNAL, 346:653–674, 1989 November 15

INTERSTELLAR MATTER IN EARLY-TYPE GALAXIES: OPTICAL OBSERVATIONS

DONG-WOO KIM
Department of Astronomy, University of California, Los Angeles
Received 1988 October 7; accepted 1989 May 11

ABSTRACT

The results of optical observations are presented for a sample of 26 early-type galaxies that are bright in the infrared. Optical broad-band imaging (using *B* and *R* filters) and narrow-band imaging (using Hα interference filters) have been performed to study dust patches and ionized gas. We have also made long-slit spectroscopy to determine gas kinematics. From direct imaging, we have detected dust lanes and ionized gas typically on a scale of 10″–20″ in more than half of our galaxy sample. The spectroscopic data confirm the presence and distribution of the interstellar matter seen in the direct imaging. The dust lanes and ionized gas are distributed in various ways—aligned along either the apparent major, or minor axis, or not even along either of them, indicating that triaxiality is in general required as a galaxy figure. Decoupled kinematics of interstellar gas and stars favors an external origin of the interstellar matter. For some isolated galaxies, however, an internal origin is not excluded.

The rotation curves determined by optical emission lines are symmetric about the center in most galaxies observed. It appears that the interstellar matter is in a circularly rotating disk around the center. Galaxy masses and mass-to-light ratios are estimated using the rotation curves of the ionized gas. A trend that the mass-to-light ratio increases with radius is found; it suggests the presence of dark matter in early-type galaxies as in spirals. Ionized gas in early-type galaxies is very often accompanied by cold gas. For most early-type galaxies in our sample, the [N II] lines are stronger than Hα, resembling the intensity ratios observed in a LINER galaxy where ionization is probably due to nuclear activity rather than stellar light. It seems that the ionized gas, and perhaps the cold gas and dust, does not directly originate in a cooling flow out of the hot X-ray–emitting gas.

Subject headings: galaxies: internal motions — galaxies: interstellar matter — galaxies: photometry

I. INTRODUCTION

Detection of interstellar matter in many early-type galaxies which were traditionally believed to be gas-free brings new insights into the study of this class of galaxies. Various phases of interstellar matter—hot X-ray–emitting gas, warm ionized gas, and cold gas—have been detected in early-type galaxies (see reviews by Schweizer 1987). Roughly half of the early-type galaxies seem to have detectable amounts of interstellar matter. Sadler and Gerhard (1986) estimated that the occurrence of dust lanes in early-type galaxies is about 40% in ellipticals and higher in S0 galaxies, and Phillips *et al.* (1986) found ionized gas in about 60% of a similar sample. The number of early-type galaxies known to have dust lanes (Ebneter and Balick 1985; Sadler and Gerhard 1985; Sparks *et al.* 1985; Gallagher 1986; Hansen, Norgaard-Nielson, and Jorgenson 1985; Bertola 1987; Mollenhoff and Bender 1987; Ebneter, Djorgovski, and Davis 1988), and ionized gas (Ford and Butcher 1979; Kent and Sargent 1979; Hansen, Norgaard-Nielson, and Jorgenson 1985; Pogge and Eskridge 1987; Sadler 1987) has rapidly increased in recent years.

In addition, the *IRAS* co-adding procedure leads to detection of far-infrared emission in about 50% of early-type galaxies in a large sample consisting of ~1100 galaxies (Jura *et al.* 1987; Knapp *et al.* 1989). The far-infrared emission is most likely explained by the thermal emission from interstellar dust, because of the infrared color temperature (~30 K) and the correlation with the H I 21 cm line emission (Jura 1986; Kim 1988). The far-infrared emission indicates that masses of cold interstellar matter are typically 10^7–10^8 $M_\odot$ in early-type galaxies. Galaxies with strong infrared emission are, therefore, candidates for detailed investigation.

In this paper, we report the results of optical observations for infrared-selected galaxies. We have performed optical broad-band imaging using *B* and *R* filters to study dust patches, and narrow-band imaging using Hα interference filters to observe ionized gas. We have also performed optical long-slit spectroscopy to determine gas kinematics and relative line ratios. The combined information concerning the distribution and kinematics of interstellar matter provides a useful tool to investigate these galaxies. The relative orientation of gas and dust in the stellar potential field gives an important clue to the structure of the galaxies (Tohline, Simonson, and Caldwell 1982; van Albada *et al.* 1982; Merritt and de Zeeuw 1983), particularly when the gas and dust are not aligned with the stellar body. The gas kinematics can be used to distinguish the origin of the gas through comparison with the stellar kinematics, and to estimate galaxy masses and mass to-light ratios. The relative line ratios (for example, the Hα-to-[N II] ratio) can be used to investigate the ionization mechanism and nuclear activity (see Baldwin, Phillips, and Terlevich 1981).

Optical observations provide a higher spatial resolution than those available at other wavelengths. Through direct imaging observations, the amount and distribution of dust and ionized gas can be determined on a scale of arcsec; the *IRAS* data only indicate the presence of dust on a scale of arcminutes, and existing H I data also only have a spatial resolution of about 1′. Small-scale imaging is particularly important for understanding the origin and evolution of interstellar matter, and fueling and reproducing the central activity by surrounding materials.

The galaxies studied here were selected on the basis of the *IRAS* data. We chose bright elliptical galaxies which are

TABLE 1

PROGRAM GALAXIES

NAME	TYPE RSA	TYPE RC2	B	DIAMETER	D (Mpc)	F (IRAS) (mJy) 12	25	60	100	F (1.4) (mJy)	F_x (ergs s^{-1} cm^{-2})	M (H I) ($M_\odot$)	M (cold) ($M_\odot$)
N0404.....	S0	E/S0	10.2	4.4	1.8	<300	260	2260	4500	...	...	0.38(8)	0.23(7)
N0524.....	S0/Sa	S0	11.6	3.2	23.8	240	<159	760	2050	...	0.24(−12)	<0.23(9)	0.19(9)
N1052.....	E/S0	E3	11.3	2.9	13.6	230	550	880	1580	560	...	0.24(9)	0.47(8)
N1060.....	...	E/S0	12.9	...	52.1	110	250	2390	4130	...	...	...	0.18(10)
N1275.....	Ep	Ep	12.4	2.6	53.0	950	2830	5760	7500	14800	0.86(−9)[a]	...	0.34(10)
N1332.....	S0	S0	11.3	4.6	13.1	100	110	510	1810	...	0.50(−12)	<0.72(9)	0.50(8)
N1400.....	E/S0	E/S0	11.8	1.9	4.4	<117	110	740	3280	...	<0.12(−12)	<0.61(7)	0.10(8)
N1407.....	E0	E0	10.7	2.5	15.9	120	<87	140	480	50	0.12(−11)	<0.42(9)	0.19(8)
N2768.....	S0	E6	11.1	6.3	18.1	80	110	390	1370	13	...	<0.69(9)	0.72(8)
N2974.....	E4	E4	11.6	3.4	22.5	160	<87	420	1900	11	0.22(−12)	0.72(9)	0.15(9)
N3415.....	E5	S0	12.8	2.4	37.4	140	130	1340	4050	...	...	...	0.91(9)
N3516.....	SB0	SB0	12.4	2.3	30.7	410	1010	1850	2130	26	...	<0.53(9)	0.32(9)
N3665.....	S0	S0	11.8	3.2	26.3	110	210	1910	7530	100	...	<0.56(10)	0.83(9)
N3894.....	...	E4	12.9	2.4	37.4	<72	130	140	480	...	<0.38(−12)	...	0.11(9)
M3928.....	...	E0	13.1	1.8	15.6	260	470	3070	5790	...	...	...	0.23(9)
N4125.....	E6	E6	10.6	5.1	18.9	<117	110	700	1670	...	...	<0.16(9)	0.95(8)
N4261.....	E3	E3	11.3	3.9	13.5	180	90	80	150	16400	...	...	0.44(7)
N4374.....	E1	E1	10.3	5.0	13.5	220	190	500	1160	6300	0.77(−12)	<0.13(9)	0.34(8)
N4589.....	E2	E2	11.6	3.0	24.8	<99	<69	200	660	35	0.18(−12)	...	0.65(8)
N4649.....	S0	E2	9.8	7.2	13.5	240	170	780	1090	25	0.32(−11)	<0.13(9)	0.32(8)
N4697.....	E6	E6	10.1	6.0	10.9	290	<123	460	1240	...	0.23(−12)	<0.65(9)	0.24(8)
N4742.....	E4	E4	12.1	2.3	11.7	<132	<148	450	1150	...	...	...	0.25(8)
N5018.....	E4	E3	11.6	2.6	31.4	200	<177	950	1860	3	...	0.43(9)	0.29(9)
N5273.....	S0/a	S0	12.4	3.1	11.6	120	290	900	1560	...	...	<0.34(8)	0.34(8)
N5322.....	E4	E3	11.1	5.5	23.8	<66	<63	420	100	87	<0.32(−12)	<0.12(10)	0.91(8)
N5576.....	E4	E	11.8	3.2	21.1	70	80	90	210	...	...	0.30(8)	0.15(8)

[a] X-ray flux (2–10 keV) from Cowie *et al.* 1983 for the Perseus cluster (A426).

detected in at least two *IRAS* bands, indicating they have interstellar matter. The 26 selected galaxies and their *IRAS* fluxes are listed in Table 1. The table gives morphological types, blue magnitudes, and diameters from the Revised Shapley-Ames Catalogue of Galaxies (Sandage and Tammann 1981, hereafter RSA) and the Second Reference Catalogue of Bright Galaxies (de Vaucouleurs, de Vaucouleurs, and Corwin 1976, hereafter RC2). The distance is estimated using the prescription of Knapp, Turner, and Cunniffe (1985), with $H_0 = 100$ km s^{-1} Mpc^{-1}. Also listed are the radio continuum fluxes from Disney and Wall (1977), Dressel and Condon (1978) and Hummel (1980), the X-ray fluxes from Forman, Jones, and Tucker (1985) and Canizares, Fabbiano, and Trinchieri (1987), the masses of H I gas from Knapp, Turner, and Cunniffe (1985) and Wardle and Knapp (1986) and the masses of cold interstellar gas estimated by the *IRAS* 100 μm flux (Jura *et al.* 1987; Knapp *et al.* 1989).

The observations were performed with the 120 inch (3 m) and 40 inch (1 m) telescopes of Lick Observatory, and details regarding the observations are described in § II. The data reduction procedures are given in § III. The results of imaging and spectroscopy are presented in § IV and are discussed in § V.

II. OBSERVATIONS

The main observations of this study were performed with the 3 m telescope of Lick Observatory from 1987 November to 1988 March. Supplementary observations were done with the 1 m telescope of Lick Observatory, especially for large galaxies because of a larger field of view available. All spectroscopic observations were made with the 3 m telescope. The observation log is given in Table 2. The typical seeing during the observing run was approximately 2″—a little better in 1988 March and a little worse in 1987 November. Most observations were made during photometric nights, but the atmospheric conditions during 1988 February 20–22 were not good; the results for a few galaxies which were only observed during this observing run are thus subject to relatively large uncertainties (see § IV). At least two images, sometimes more, were taken with each passband. All images were reduced, and then the images with the best quality were used for the following discussions.

The CCD used in this study was a Texas Instruments 800 × 800 CCD for the 3 m telescope. The pixel size is 0.″71 in a lens-grism mode and 0.″66 in a grating mode. The size of field for direct imaging is about 200 × 200 pixels (800 × 200 for spectra), therefore the field of view is about 2′ × 2′. By suitably choosing the placement of an image on the whole chip, some bad columns in the CCD could be avoided. For the 1 m telescope, a TI 500 × 500 CCD was used. Its pixel size 0.″54 and the field of view is 4.′5 × 4.′5, which is larger than that available with the 3 m telescope.

To get $B-R$ images, broad-band B and R filters were used. The B filter consists of three filters, BG-18 (1 mm), GG-385 (2 mm), and BG-12 (1 mm). The R filter is the "night-sky" filter which has a passband of 6100–7600 Å and blocks most of the artificial night sky lines (for details of calibration of the R filter, see Djorgovski 1985). Both of the filters are slightly narrower than the Johnson B and R filters. Since we are not interested in the B and R magnitudes but rather in the $B-R$ color excess, we do not transform our results into the Johnson standard system.

TABLE 2

OPTICAL OBSERVATION LOG

Name	1987 Nov 16–18[a,b]	1988 Feb 20–22[a,c]	1988 Mar 14–16[a,c]	1988 Mar 17–19[d,e]
N404.....	BRLC	...	...	...
N524.....	BRLC	...	...	...
N1052.....	BRLC	...	...	...
N1060.....	BRLC	...	BRLC SP90	...
N1275.....	BRLC	BR SP90	..	...
N1332.....	BRLC	...	...	...
N1400.....	...	BR SP90	BRLC SP90	...
N1407.....	BRLC	SP90	SP90	...
N2768.....	...	BRLC SP90/0	BRLC	...
N2974.....	BRLC	BRLC SP44/90	...	BR
N3415.....	...	...	BRLC	...
N3516.....	...	BRLC SP90/0	...	...
N3665.....	...	...	BRLC SP30/120	...
N3894.....	...	...	BRLC SP11	BRLC
N3928.....	...	...	BRLC SP90/0	BRLC
N4125.....	...	BRLC SP90/0	LC SP90/0	...
N4261.....	...	BRLC	LC SP60/150	...
N4374.....	BRLC	LC	SP90/0	...
N4589.....	...	BRLC	BRLC SP95/5	...
N4649.....	...	BRLC	LC SP90	BR
N4697.....	...	BRLC SP65	BR	...
N4742.....	...	BRLC	BRLC SP90	...
N5018.....	...	BRLC SP90	...	BR
N5273.....	...	BRLC SP0	BRLC SP90/0	...
N5322.....	...	BRLC SP90	BRLC SP90/0	...
N5576.....	...	...	BRLC SP90	...

NOTE.—B: *B* image; R: *R* image; L: line image; C: continuum image; SP: spectrum at the position angle of the following number.

[a] 3 m telescope.

[b] UV Schmidt.

[c] Lens/grism.

[d] 1 m telescope.

[e] Direct.

Narrow-band filters (full width of 70–80 Å) were selected for the redshift of each galaxy. The central wavelengths and bandpasses of the filters used are listed in Table 3. These filters cover the Hα and [N II] λ6548 + λ6584 lines. However, NGC 3516 has a very broad Hα component ($\Delta\lambda \sim 150$ Å), and hence two images were taken with two adjacent filters. The filters for line-free continuum were selected either blueward or redward from the lines, and special precautions were taken not to include nearby [S II] λ6713 and λ6737 lines.

All the spectra were taken in a grism mode. The grism that we employed is centered at 6500 Å with a range of 1880 Å and a wavelength resolution of 2.65 Å pixel^{-1}. The employed slit is 2″ (3 pixels) wide and about 2′ long. For each galaxy, spectra were taken with two slit positions, along the major and minor axes of the galaxy. In NGC 4374, where the ionized gas is distributed along the skewed axis, spectra were taken with slit positions along and perpendicular to the gas distribution.

In each observing run, flat-field images were taken by using dome light and blank fields of sky near sunset and sunrise for each broad-band and narrow-band filter separately. Then average images for each filter were used to correct variation in CCD response. For absolute calibration, several standard stars from Oke (1974) and Stone (1977) were observed each night.

III. DATA REDUCTION

To analyze the data, the Vista program which was developed at Lick Observatory for CCD data reduction was used. Sky brightness was usually estimated from the corners of the field containing an object in the center. For galaxies which are larger than the field of view (for example, NGC 2768 and NGC 4649), sky images were separately taken with the same exposure times as for the galaxies after slightly changing the telescope position.

To find dust lanes, *R* images are divided by *B* images. The resulting images correspond to $B-R$. Before division, one image is shifted to match the other. Shifting is sometimes very critical, and we tried to shift to an accuracy of one-tenth of a pixel size to achieve the best match. To find ionized gas, images for the line and line-free continuum were taken separately, and the continuum image was subtracted from the line plus continuum image after being shifted and adjusted for differences in filter response. The direct imaging provides total intensities of Hα and [N II] lines convolved with the filters used. Then, to deconvolve the filter response, i.e., to correct for nonperfect transparency of the filter within the passband, we use the spectrum which was taken at a position angle along the distribution of the ionized gas. For NGC 404 and NGC 1052, the spectra made by Filippenko and Sargent (1985) were used as calibrators. The estimated line intensities and line ratios are summarized in Table 5. The typical error of the line fluxes involved in correcting atmospheric extinctions and transferring to absolute fluxes is less than 10%. However, some observations were made during bad atmospheric conditions, particularly in 1988 February. In this case (NGC 2974 and NGC 4374), the error could be as large as 30%; the fluxes subject to larger errors are marked by colons in Table 5.

TABLE 3

NARROW-BAND FILTERS

Name	Line	Continuum
N404.....	6563(75)	6649(76)
N524.....	6606(80)	6693(77)
N1052.....	6606(80)	6693(77)
N1060.....	6693(77)	6606(80)
N1275.....	6693(77)	6606(80)
N1332.....	6606(80)	6693(77)
N1400.....	6570(70)	6649(76)
N1407.....	6606(80)	6693(77)
N2768.....	6606(80)	6693(77)
N2974.....	6606(80)	6693(77)
N3415.....	6649(75)	6570(70)
N3516.....	6606(80)	6693(77)
	6649(76)	6520(75)
N3665.....	6606(80)	6693(77)
N3894.....	6649(76)	6570(70)
	...	6520(75)
N3928.....	6606(80)	6693(77)
	...	6649(76)
N4125.....	6606(80)	6693(77)
N4261.....	6606(80)	6693(77)
N4374.....	6606(80)	6693(77)
N4589.....	6606(80)	6693(77)
N4649.....	6606(80)	6693(77)
N4697.....	6606(80)	6693(77)
N4742.....	6606(80)	6693(77)
N5018.....	6649(76)	6520(75)
N5273.....	6606(80)	6693(77)
N5322.....	6606(80)	6693(77)
N5576.....	6606(80)	6693(77)

Small errors in one frame which do not exist in another frame may generate some arbitrary features after subtraction or division of the two unmatched images. The main problem would be caused by variation of seeing during the two exposures, and possibly by focusing and tracking, especially in a long exposure. The error caused by the latter two effects is usually better than the typical seeing ($\sim 2''$). Some galaxies are known from the previous studies to contain dust and/or ionized gas; NGC 1052 (Sparks *et al.* 1985), NGC 2974 (Demoulin-Ulrich, Butcher, and Boksenberg 1985) and NGC 4374 (Hansen, Norgaard-Nielson, and Jorgenson 1985). For these galaxies we could reproduce the same distribution of dust lanes and ionized gas as those found by the previous observers (for detailed comparison, see the descriptions for individual galaxy).

For wavelength calibration, a Ne lamp was used. After transforming spectra to a linear scale, night sky lines were used for each spectrum to correct the zero point of the wavelength scale. For the observing run in 1988 March, the zero point shift is always less than 1 Å, which is smaller than the wavelength resolution. However, for the run in 1988 February, the zero point shift is up to 10 Å; hence the central velocities are subject to larger uncertainties. However, velocity gradients which are used to derive rotation curves are not significantly affected. NGC 4125 was observed in both runs and its difference of zero points after shifting by the sky lines is only 18 km s^{-1} The central velocity is measured at the position where the line intensity peaks. The uncertainty in the velocity is mainly due to the error of the zero point, and it is less than 50 km s^{-1} (about 1 Å) except for those observed in 1988 February, which have a higher uncertainty.

To measure a rotation velocity, we used the strongest line, either Hα or [N II]. After wavelength calibration, the position of the line peak was measured in an accuracy 0.1 Å for each slice with a step of $0''.71$ along the slit. The typical error in the velocity is about 20–30 km s^{-1} in the central part and 50 km s^{-1} in the outer part, where the line intensity becomes weak.

IV. RESULTS

We have detected dust lanes and ionized gas in 12 galaxies (though not always gas and dust in the same objects) out of 23 galaxies. In Figures 1–11, we show the contour plots of *B* and *R* images as well as $B-R$ and line (Hα + [N II]) images after continuum subtraction. The contour maps of emission lines from NGC 1275, and the three galaxies with spiral-shaped ionized gas (see below) are shown in Figure 12. In the contour plots of the *B* and *R* images, each step is in 0.5 mag difference (a factor of 1.583), and the zero point is arbitrary. In the contour plots of the $B-R$ and emission lines, contour levels are given in each plot.

In Table 4, the characteristics of detected dust lanes and ionized gas are summarized. To detect dust lanes, we look for differences between the *B* and *R* images. The presence of dust lanes mainly causes the following differences in the *B* and *R* isophotes.

1. Isophote distortion is seen in the light distribution. The distortion is more pronounced in the *B* image than in the *R* image. Sometimes the isophote in the *R* image even appears normal. This is the most direct way to determine dust lanes. NGC 2768, NGC 4374, and NGC 4589 are examples. Even stronger distortion is seen in NGC 404 and NGC 3665, where distortion is clearly seen in all the passbands.

2. There is a different degree of isophote twisting in the *B* and *R* images. It is usually accompanied by other aspects and

TABLE 4

SUMMARY OF OPTICAL IMAGING

Galaxy	Remarks
N404.....	Strong dust lane along the skewed axis and ionized gas along the major axis
N1052.....	Dust lane and ionized gas roughly along minor axis
N1275.....	Filamentary distribution of ionized gas
N2768.....	Dust lane along the minor axis and ionized gas gas in the center
N2974.....	Dust lane and ionized gas along the major axis
N3665.....	Strong off-center dust lane and ionized gas along the major axis
N3894.....	Dust lane and ionized gas along the major axis
N4125.....	Dust lane and ionized gas along the major axis
N4261.....	Dust lane along the major axis and ionized gas in the center
N4374.....	Dust lane and ionized gas along the skewed axis
N4589.....	Dust lane and ionized gas along the minor axis
N5018.....	Dust lane to the north-west of the center
N5273.....	Dust in the east half of the galaxy and ionized gas in the center
N3415.....	Spiral structure in Hα + [N II] line image
N3516.....	Spiral structure in Hα + [N II] line image
N3928.....	Spiral structure and double peaks in Hα + [N II] line image

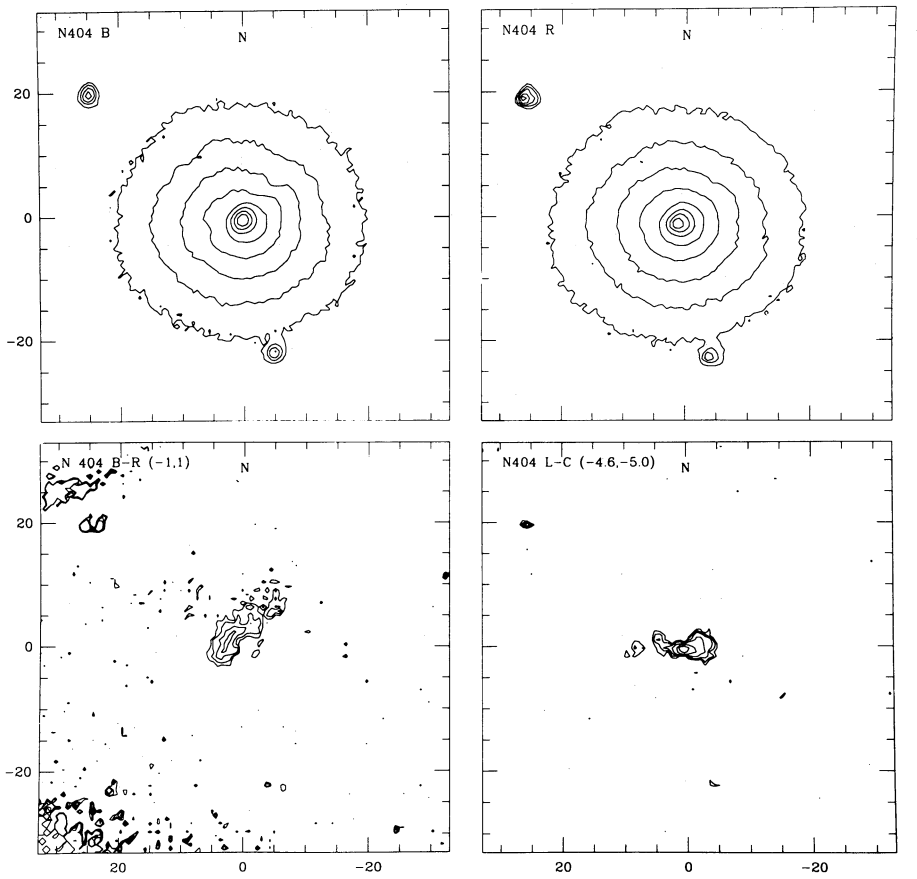

FIG. 1.—*B* (*top left*), *R* (*top right*), (*B*−*R*) (*bottom left*), and line (*bottom right*) images of NGC 404. The contour levels in *B* and *R* are in a step of 0.5 mag (a factor of 1.583), and the zero points are arbitrary. The contour levels in the *B*−*R* image are (0.1, 0.15, 0.22, 0.24) mag in *E*(*B*−*R*). The contour levels in the line image are (1.0, 3.0, 8.1, 23.4) × 10^{-16} ergs s^{-1} cm^{-2} Hz^{-1} $arcsec^{-2}$.

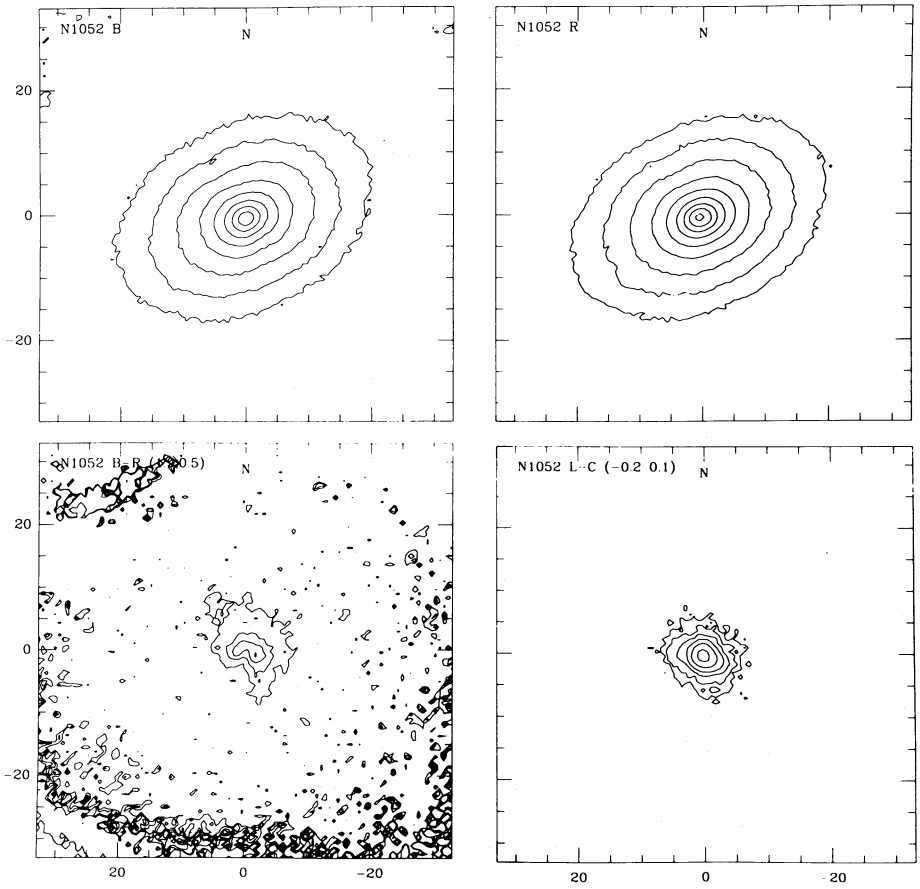

FIG. 2.—NGC 1052. Same as Fig. 1. The contour levels in *B*−*R* are (0.044, 0.13, 0.21, 0.28) mag in *E*(*B*−*R*). The contour levels in the line image are (6.4, 12.7, 25, 50, 127, 380) × 10^{-16} ergs s^{-1} cm^{-2} Hz^{-1} $arcsec^{-2}$.

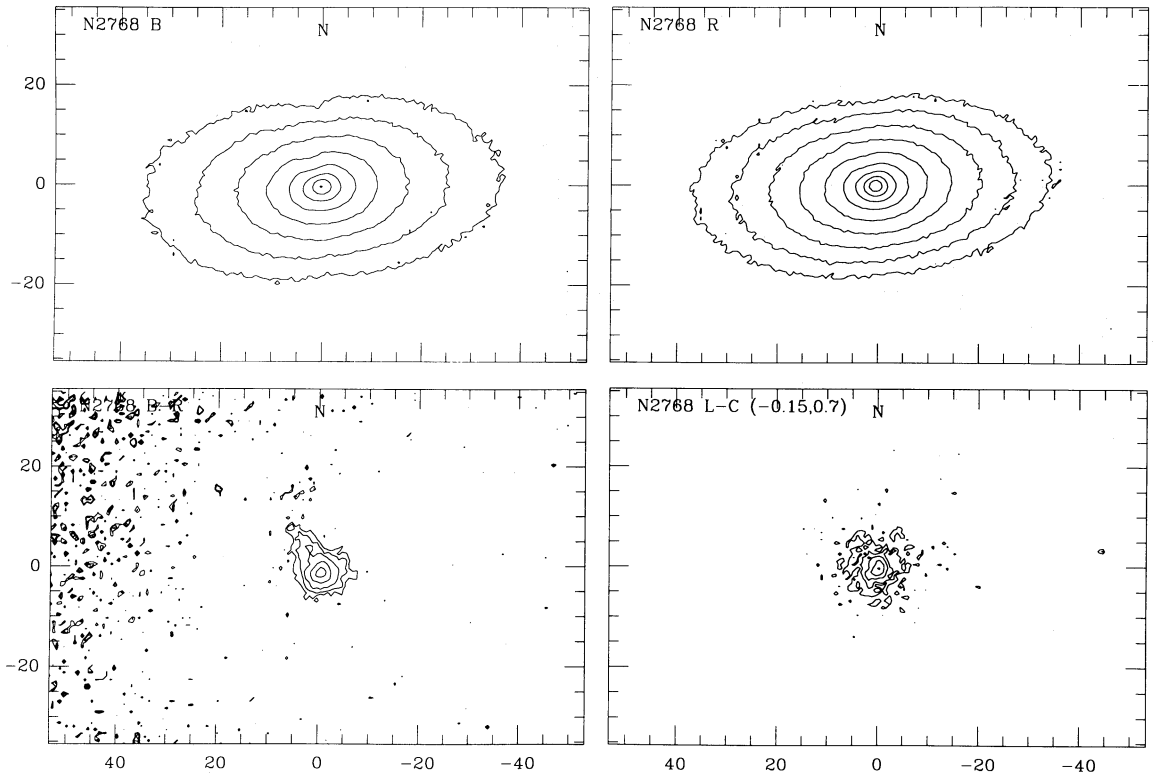

FIG. 3.—NGC 2768. Same as Fig. 1. The contour levels in $B-R$ are (0.066, 0.10, 0.14, 0.24, 0.37) mag in $E(B-R)$. The contour levels in the line image are (1.3, 3.1, 6.6, 21.9, 65.8) $\times 10^{-16}$ ergs s^{-1} cm^{-2} Hz^{-1} arcsec^{-2}.

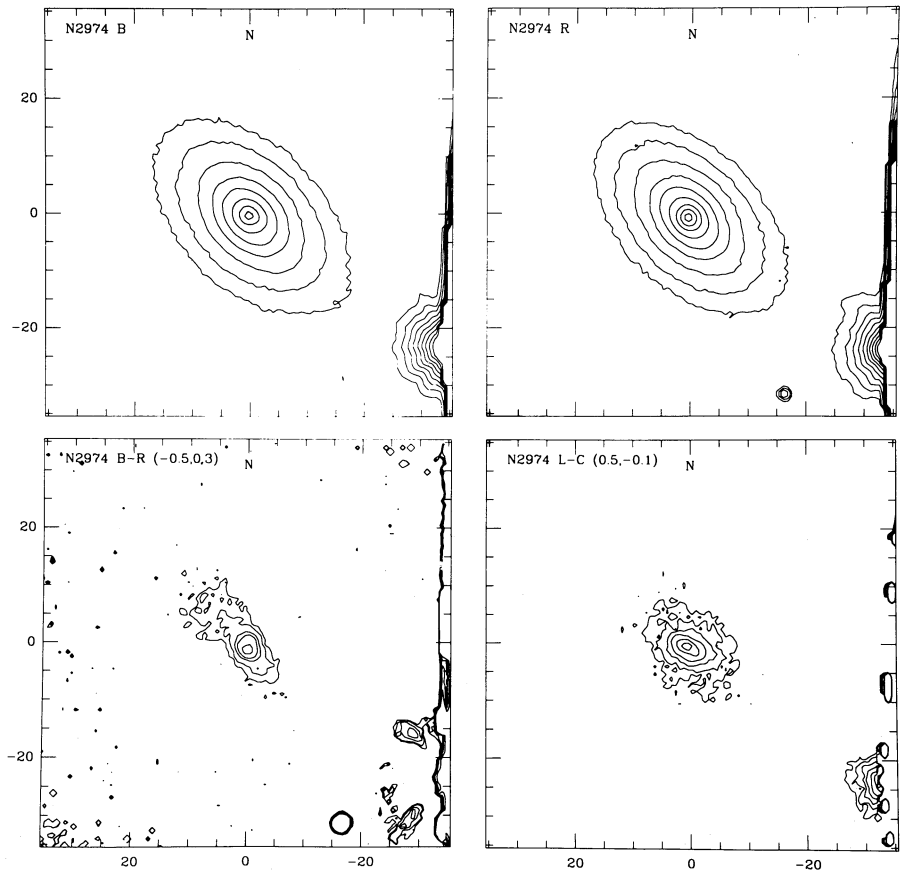

FIG. 4.—NGC 2974. Same as Fig. 1. The contour levels in $B-R$ are (0.058, 0.094, 0.18, 0.26, 0.40) mag in $E(B-R)$. The contour levels in the line image are (4.4, 8.8, 18.4, 36.7, 73.5, 147) $\times 10^{-16}$ ergs s^{-1} cm^{-2} Hz^{-1} arcsec^{-2}.

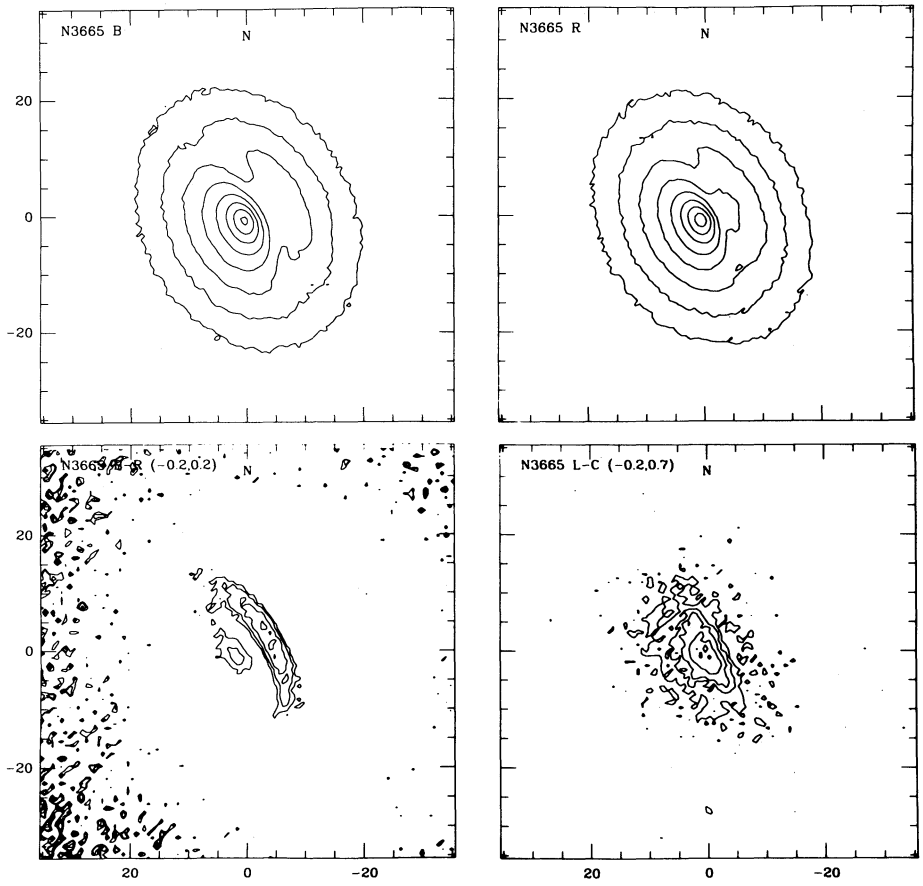

FIG. 5.—NGC 3665. Same as Fig. 1. The contour levels in $B-R$ are (0.13, 0.19, 0.27, 0.35) mag in $E(B-R)$. The contour levels in the line image are (1.79, 4.31, 7.18, 14.4, 28.7) $\times 10^{-16}$ ergs s^{-1} cm^{-2} Hz^{-1} $arcsec^{-2}$.

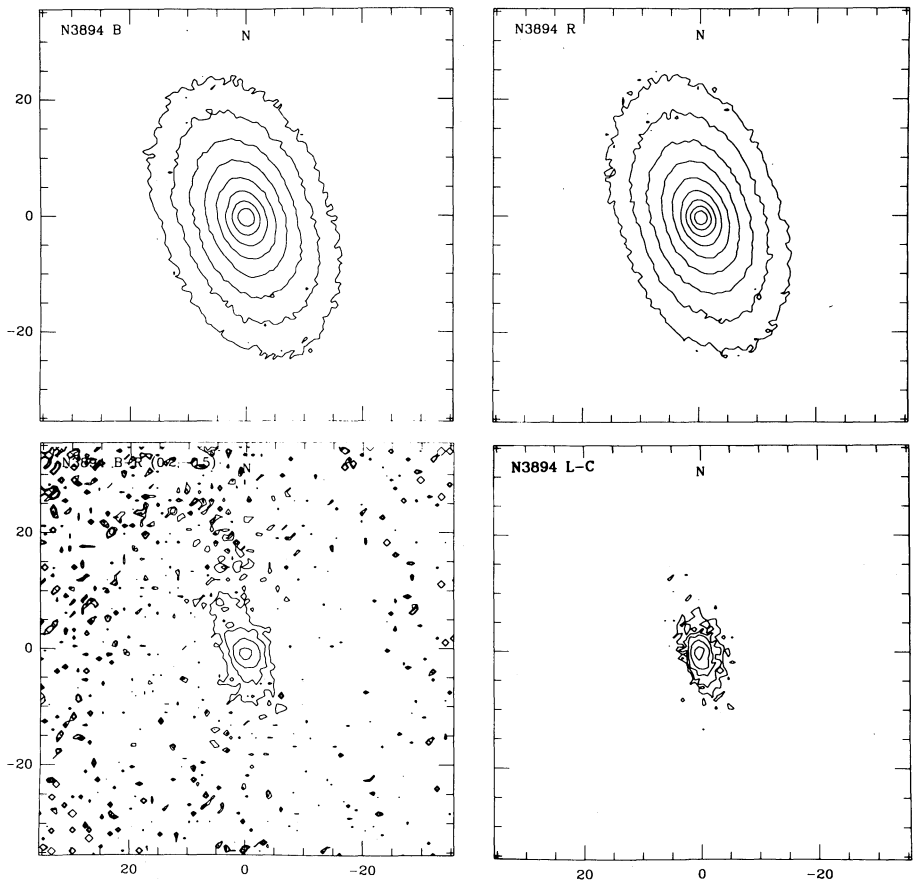

FIG. 6.—NGC 3894. Same as Fig. 1. The contour levels in $B-R$ are (0.062, 0.12, 0.23, 0.46) mag in $E(B-R)$. The contour levels in the line image are (1.2, 2.4, 4.8, 9.6, 24) $\times 10^{-16}$ ergs s^{-1} cm^{-2} Hz^{-1} $arcsec^{-2}$.

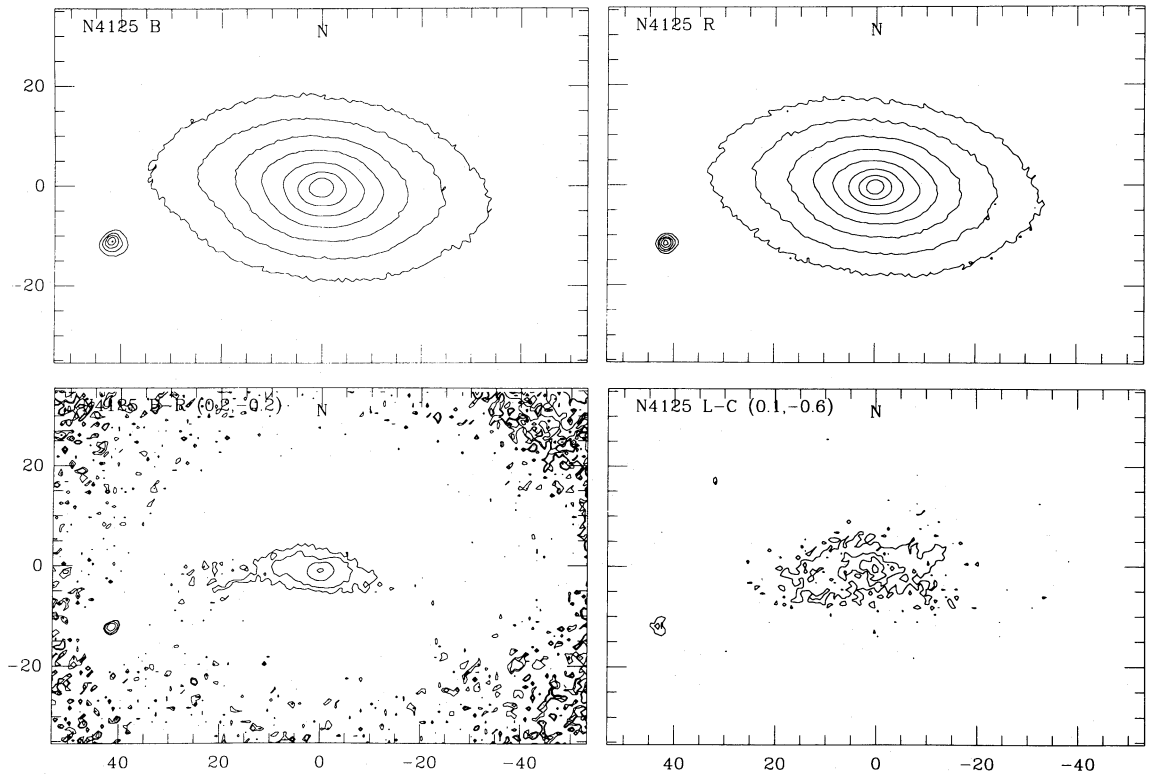

FIG. 7.—NGC 4125. Same as Fig. 1. The contour levels in $B-R$ are (0.079, 0.14, 0.30, 0.58) mag in $E(B-R)$. The contour levels in the line image are (2.6, 7.9, 15.8, 36.8) $\times 10^{-16}$ ergs s^{-1} cm^{-2} Hz^{-1} arcsec^{-2}.

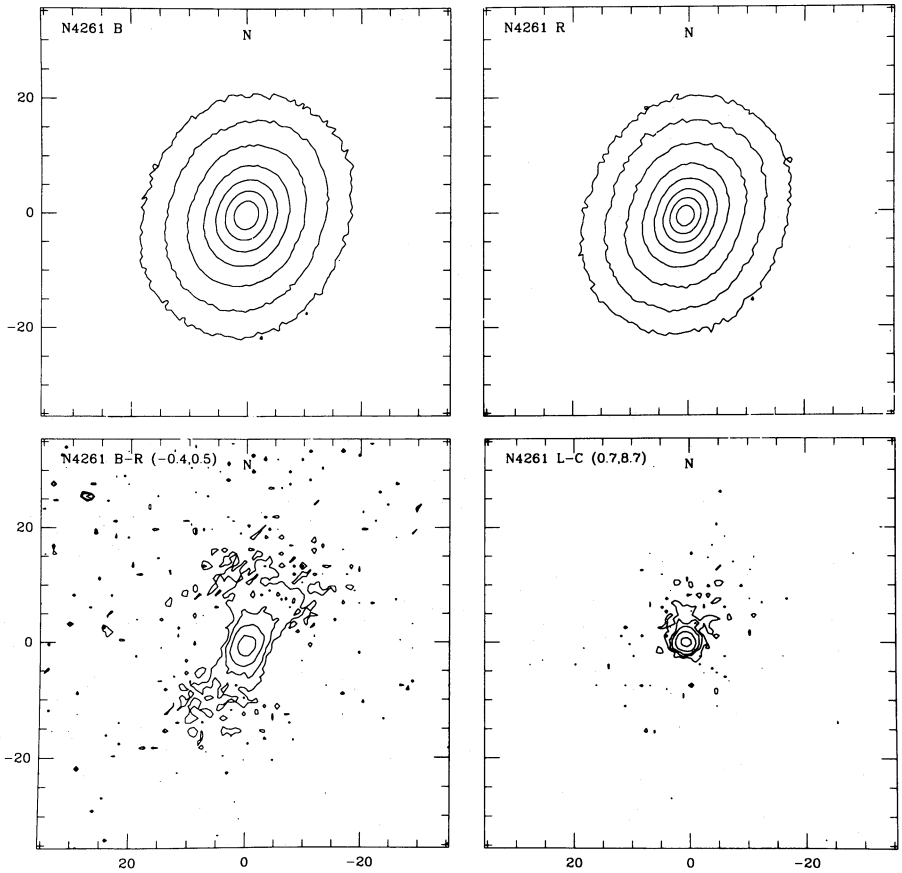

FIG. 8.—NGC 4261. Same as Fig. 1. The contour levels in $B-R$ are (0.036, 0.087, 0.17, 0.31) mag in $E(B-R)$. The contour levels in the line image are (2.0, 4.9, 9.8, 24.5, 73.5) $\times 10^{-16}$ ergs s^{-1} cm^{-2} Hz^{-1} arcsec^{-2}.

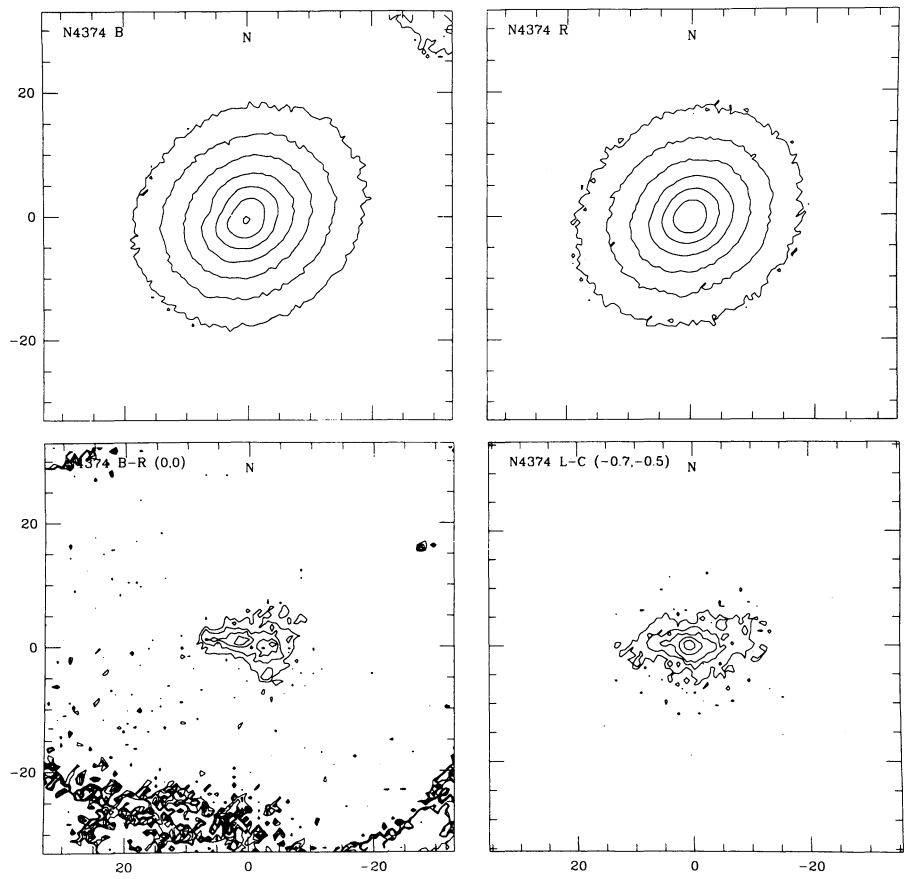

FIG. 9.—NGC 4374. Same as Fig. 1. The contour levels in $B-R$ are (0.007, 0.092, 0.14, 0.18) mag in $E(B-R)$. The contour levels in the line image are (4.9, 14.7, 29.4, 58.8, 98.0) $\times 10^{-16}$ ergs s^{-1} cm^{-2} Hz^{-1} $arcsec^{-2}$.

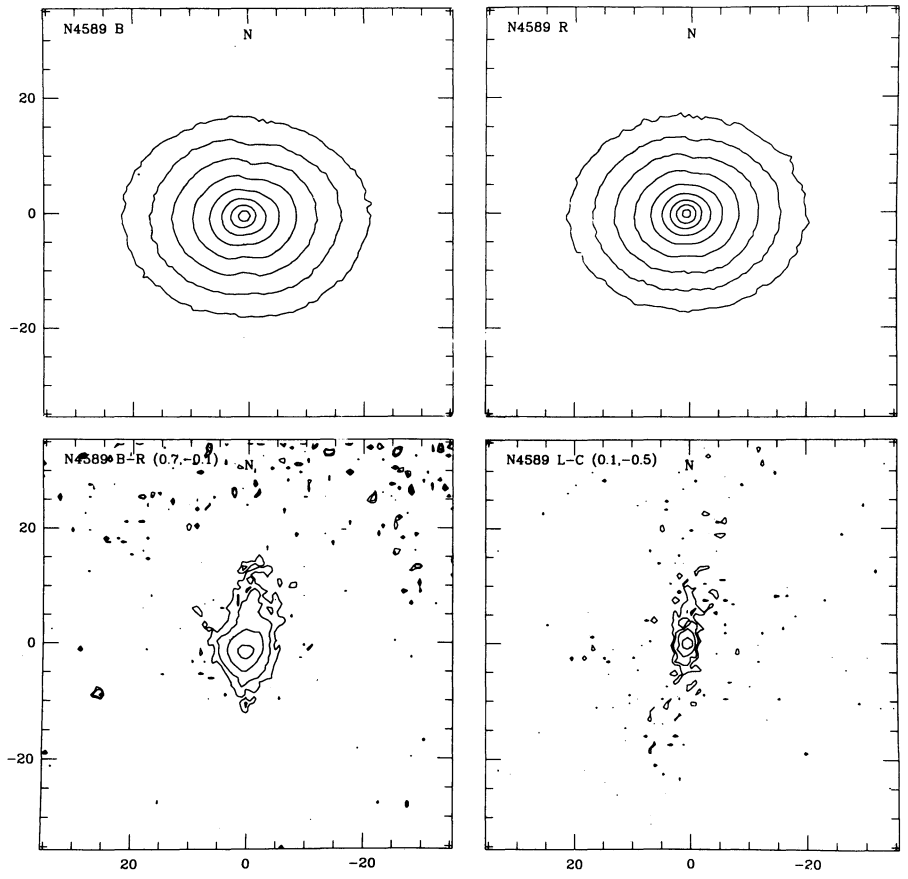

FIG. 10.—NGC 4589. Same as Fig. 1. The contour levels in $B-R$ are (0.057. 0.093, 0.18, 0.33) mag in $E(B-R)$. The contour levels in the line image are (1.5, 3.76, 9.4, 30.0) $\times 10^{-16}$ ergs s^{-1} cm^{-2} Hz^{-1} $arcsec^{-2}$.

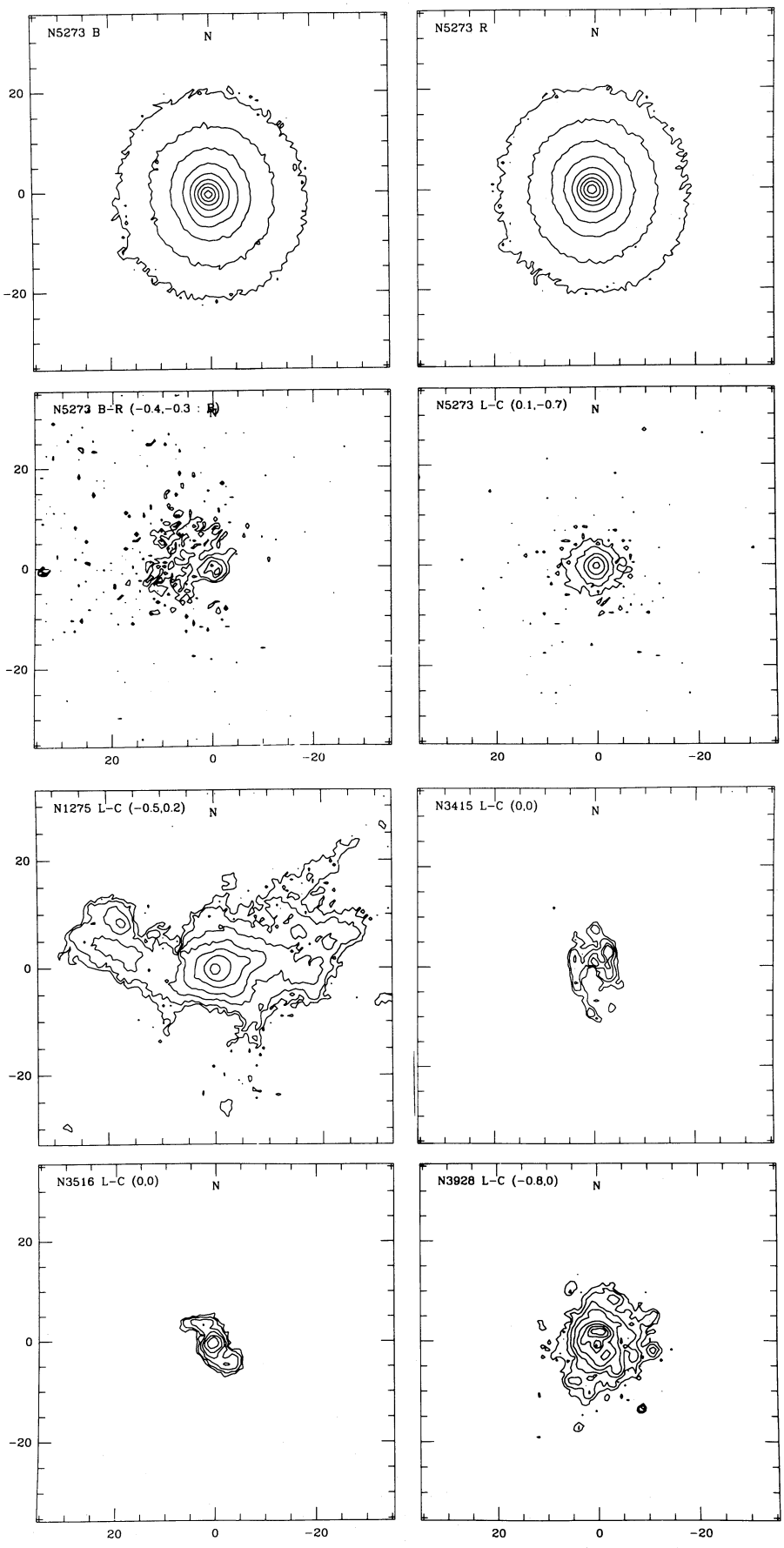

FIG. 11.—NGC 5273. Same as Fig. 1. The contour levels in $B-R$ are (0.054, 0.093, 0.16, 0.19) mag in $E(B-R)$. The contour levels in the line image are (1.5, 5.0, 14.9, 49.7, 198.8) $\times 10^{-16}$ ergs s^{-1} cm^{-2} Hz^{-1} $arcsec^{-2}$.

FIG. 12.—*Top left*: Line image of NGC 1275 after continuum subtraction. The contour levels are (4.2, 7.1, 14.1, 28.2, 56.5, 141, 706) $\times 10^{-16}$ ergs s^{-1} cm^{-2} Hz^{-1} $arcsec^{-2}$. *Top right*: Line image of NGC 3415. The contour levels are (6.2, 8.3, 12.5, 16.6) $\times 10^{-16}$ ergs s^{-1} cm^{-2} Hz^{-1} $arcsec^{-2}$. *Bottom left*: Line image of NGC 3516. The contour levels are (11, 18.4, 36.8, 73.5, 184, 551) $\times 10^{-16}$ ergs s^{-1} cm^{-2} $arcsec^{-2}$. *Bottom right*: Line image of NGC 3928. The contour levels are (1.8, 3.6, 7.2, 14.4, 35.9, 72.8, 144, 215) $\times 10^{-16}$ ergs s^{-1} cm^{-2} Hz^{-1} $arcsec^{-2}$.

virtually all dust lane galaxies have this effect. Distinct examples are NGC 1052 and NGC 4374. The isophote twisting would be interpreted as evidence of triaxiality if the twisting is the same in both B and R images.

3. In some cases, the R image is more eccentric than the B image. It is usually seen in galaxies with the major axis dust lanes. In this case, no distortion of isophotes is seen and the galaxy looks normal in each band. NGC 2974, NGC 4125, and NGC 4261 are such galaxies.

The dust lanes are distributed in various ways from one galaxy to another. NGC 2974, NGC 3665, NGC 3894, NGC 4125, and NGC 4261 have dust lanes along the apparent major axes, and NGC 1052, NGC 2768, and NGC 4589 along the apparent minor axes, and NGC 404 and NGC 4374 along skewed axes. Also note that the dust lanes in NGC 404 and NGC 3665 do not pass through the center of the galaxies, and in NGC 5018 and NGC 5273 dust is irregularly distributed (see below for details of each galaxy). For the galaxies where we could not detect any feature, isophotes in two images ($B-R$ and line-continuum) are very similar to each other, and no isophote distortion is seen. However, a face-on distribution of dust may not be excluded, since the sensitivity of our observations does not allow detection of such a feature.

In our sample galaxies, ionized gas is detected in all dust lane galaxies, and a dust lane is detected in all galaxies with emission lines. This indicates that the origins of cold and warm gas may be related. The only exception is NGC 1275. Since the R image for NGC 1275 is affected by strong emission lines, the presence of a dust lane is not clearly revealed in $B-R$. However, the strong far-infrared emission (Jura *et al.* 1987) implies the presence of cold gas and dust in this galaxy. Ionized gas is distributed more or less in a similar way as the dust lane, whether or not the distribution of dust follows that of the stellar body—see NGC 2974 (major axis dust lane), NGC 4374 (skewed axis dust lane), and NGC 4589 (minor axis dust lane). In NGC 404 and NGC 3665, both dust lanes and ionized gas are seen, but they are distributed in different ways. The very strong dust lanes probably obscure the emission from the ionized gas. NGC 2768, NGC 4261, and NGC 5273 have ionized gas only in the central core, while their dust lanes are extended.

We have also found spiral-like structures in emission line images of NGC 3415, NGC 3516, and NGC 3928 (Fig. 12). Since the isophotes of these three galaxies look quite unusual for early-type galaxies, the images in all bands are shown in Figures 13–15. While the outer most isophotes are roughly elliptical, they are far from the simple form in the inner region. The isophotes are distorted and even twisted, most strongly in the line images. As noted by Tanaguchi and Watanabe (1987) for NGC 3928 (see also van den Bergh 1980), these galaxies seem to have mini-spiral structures embedded in large bulges. Although these galaxies have been classified as E or S0 in RSA and RC2, they may belong to a new class of galaxies, i.e., bulge-dominated compact spiral galaxies. The enhanced line emission in these galaxies is most probably due to star formation as revealed by the relative line ratios (see below). Also note

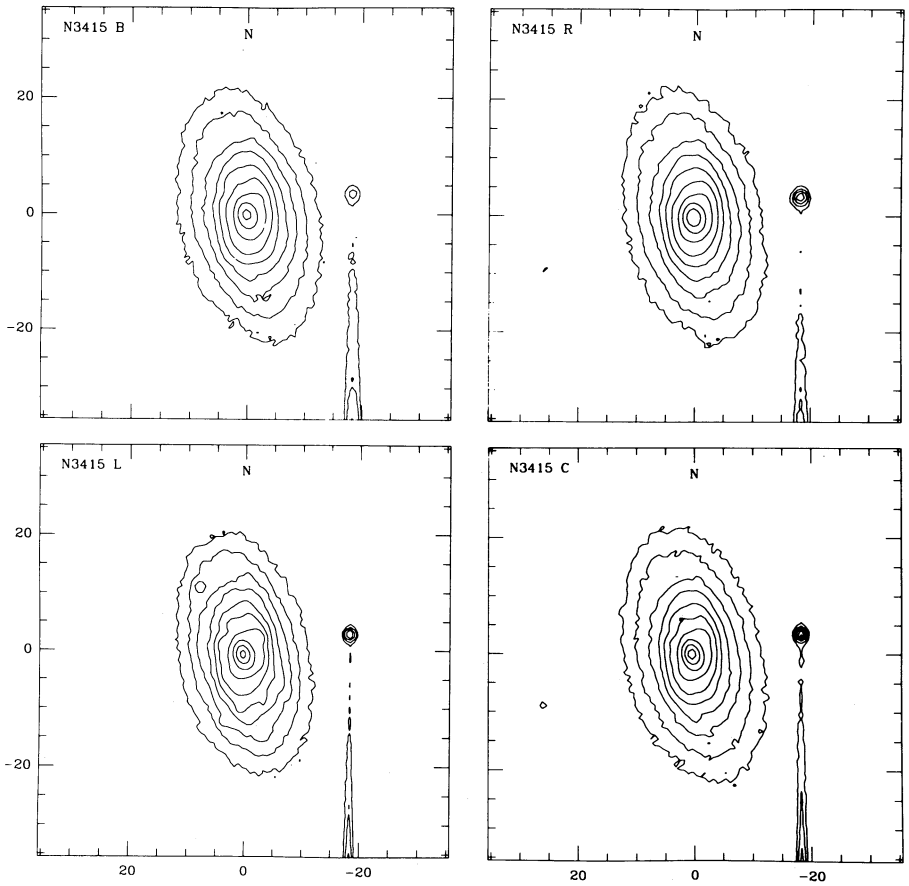

FIG. 13.—B, R, line, and continuum images of NGC 3415. The contour levels are in a step of 0.5 mag (a factor of 1.583), and the zero points are arbitrary.

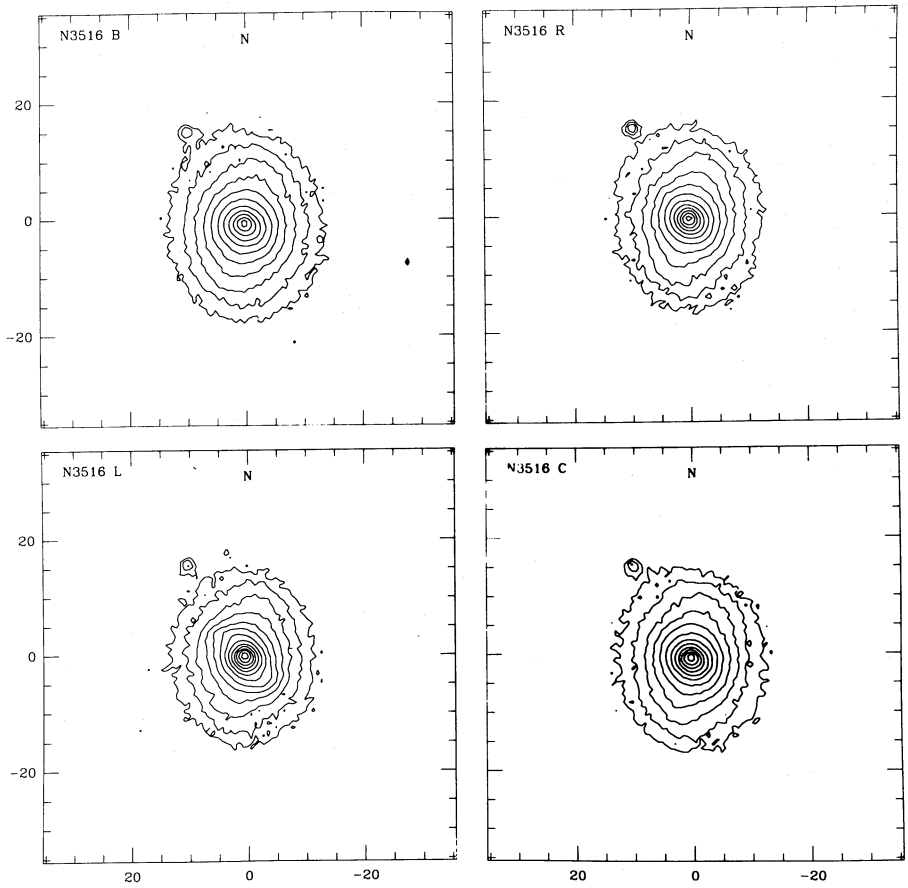

FIG. 14.—NGC 3516. Same as Fig. 13.

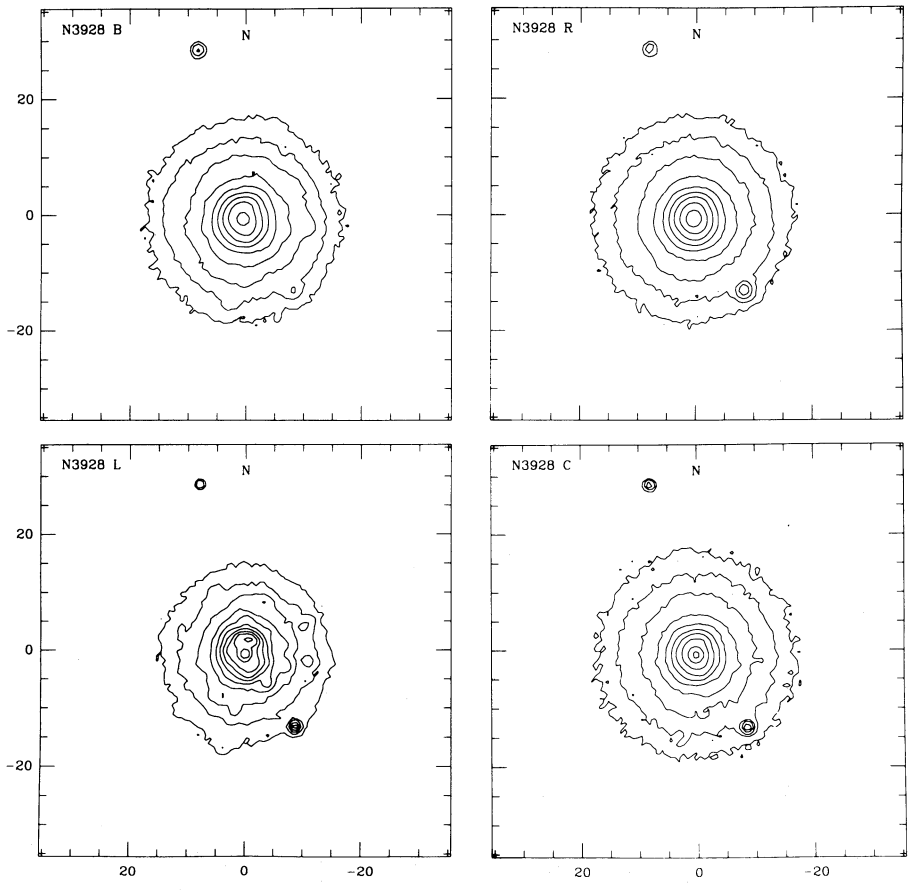

FIG. 15.—NGC 3928. Same as Fig. 13.

that the *B* images are a little bit closer to the line images than the *R* (or continuum) images; i.e., where the ionized gas resides, the light is bluer. It suggests the presence of young stars, although bright OB stars are not resolved except those to the west and to the north of the center in NGC 3928.

Spectra for line-emitting galaxies are presented in Figures 16*a*–16*l*, where emission lines (Hα, [N II] λ6548, λ6584, and [S II] λ6713, λ6737) from ionized gas are shown. The line intensity and intensity ratio of [N II] λ6584 to Hα are listed in Table 5. Excepting NGC 3516 and NGC 3928, both of which have the spiral-shaped structures in emission-line images, and NGC 3665, for early-type galaxies in the sample, the [N II] lines are stronger than Hα over the full extent of the observed line emission. This line ratio is particularly interesting because it can be used to discriminate ionization mechanisms (for example, see Baldwin, Phillips, and Terlevich 1981). If the gas is ionized by stellar radiation, as in a Galactic H II region, we would observe Hα lines stronger than [N II] lines. The observed line ratios are not compatible with this mechanism. Rather the line ratios resemble those of the LINER type activity—$F([\mathrm{N\ II}])/F(\mathrm{H}\alpha) > 0.7$ in active galaxies (Heckman 1980; Baldwin, Phillips, and Terlevich 1981; Keel 1985). If the central activity is generated by a massive central object being fueled by infalling material (see Rees 1984), at least the requirement of fueling gas is satisfied for these galaxies.

The intensity ratios of the two [S II] lines are roughly unity in all 12 galaxies. This is quite typical for line-emitting early-type galaxies (Demoulin-Ulrich, Butcher, and Boksenberg 1984; Phillips *et al.* 1986). Since the [S II] line ratio is sensitive to density, the similarity in the [S II] line intensities indicates an electron density of about 1000 cm^{-3} (Osterbrock 1974). Assuming an electron density of 1000 cm^{-3}, and using the case B recombination theory (Osterbrock 1974), masses of H II gas can be determined by

$$M_{\mathrm{H\ II}}(M_\odot) = 2.8 \times 10^2 \left(\frac{D}{10\ \mathrm{Mpc}}\right)^2 \times \left(\frac{F(\mathrm{H}\alpha)}{10^{-14}\ \mathrm{ergs\ s^{-1}\ cm^{-2}}}\right)\left(\frac{10^3\ \mathrm{cm^{-3}}}{n_e}\right).$$

The estimated masses of ionized gas are listed in the last column of Table 5. The typical H II gas mass is about 10^3–10^4 $M_\odot$, except in NGC 1275 and the three galaxies with the spiral-like emission region, where the ionized gas mass is larger by approximately an order of magnitude.

TABLE 5

LINE INTENSITY

Name	$F(\mathrm{H}\alpha + [\mathrm{N\ II}])$ (ergs $\mathrm{s^{-1}\ cm^{-2}}$)	$F([\mathrm{N\ II}])/F(\mathrm{H}\alpha)$	M(H II) ($M_\odot$)
N404.....	1.5×10^{-13}	0.6[a]	8.6×10^1
N1052.....	8.1×10^{-13}	1.1[a]	2.0×10^4
N1275.....	3.2×10^{-12}	1.1	1.2×10^6
N2768.....	7.5×10^{-14}	2.8	1.9×10^3
N2974.....	3.1×10^{-13}	2.7	1.1×10^4
N3415.....	1.9×10^{-13}	...	3.7×10^4[b]
N3516.....	2.4×10^{-12}	0.9	3.5×10^5
N3665.....	8.5×10^{-14}	0.8	9.2×10^3
N3894.....	7.3×10^{-14}	2.2	9.0×10^3
N3928.....	8.5×10^{-13}	0.4	4.2×10^4
N4125.....	1.6×10^{-13}	>3.5	$<2.4 \times 10^3$
N4261.....	9.6×10^{-14}	>3.5	$<1.1 \times 10^3$
N4374.....	2.1×10^{-13}	3.2	2.6×10^3
N4589.....	4.7×10^{-14}	2.1	2.6×10^3
N5273.....	2.1×10^{-13}	1.4	3.3×10^3

[a] Estimated from the spectra in Filippenko and Sargent 1985.
[b] $F([\mathrm{N\ II}]\ \lambda6584)/F(\mathrm{H}\alpha) = 1$ is assumed.

The ionized gas is often extended to 10″–15″, permitting measurement of rotation velocities for these galaxies. In all cases, the gas kinematics is consistent with the direct imaging data in the sense that the rotation axis is perpendicular to the distribution of the ionized gas. And the extent of line emission along the two perpendicular directions is roughly consistent with the size of the ionized gas distribution as determined by the direct imaging. Therefore, the spectroscopic data confirm the various distributions of dust and ionized gas; along the major axis, minor axis or skewed axis seen in the direct imaging. For NGC 3928 and NGC 5273, velocity changes are detected along neither the major nor the minor axis. NGC 3928 seems to be almost face-on (van den Bergh 1980), and gas in NGC 5273 is centrally concentrated. The results of nine galaxies are shown in Figures 17*a*–17*i*, where the position angle of the slit and the orientation are marked in each rotation curve.

Except for NGC 4261, where the ionized gas is concentrated in the center so that only the rising portion of a rotation curve is measured, the ionized gas reveals the rotation curve up to the turning point. Also the observed rotation curve is symmetric about the center in most galaxies observed in this study; the rotation velocity rapidly increases to a maximum within the central few arcsec and then either remains constant out to the last observing point or slightly drops after the maximum. However, NGC 3894 has quite an abnormal rotation curve, and NGC 4374 has a slightly asymmetric rotation curve. The peak velocity of emission lines is compared with the stellar velocity adopted from Knapp *et al.* (1989) in Table 6. Within the uncertainties in both measurements, the velocities are consistent with each other. The rotation velocity and radius at which it is measured are then listed in Table 6.

From the rotation curve of the ionized gas, we estimate the mass within a given radius by assuming circular rotation. We used the distribution of ionized gas seen in the optical imaging to correct the inclination effect according to the apparent axial ratio, $\cos(i) = b/a$. The estimated mass inside the radius is listed in the last column of Table 6. In NGC 2768 and NGC 4261, the ionized gas is seen only in the center; hence, we could not estimate the inclination. Only limits for the masses are given for these galaxies.

a) NGC 404

NGC 404 has one of the strongest dust lanes in our sample. The isophote in the *B* image is heavily distorted and even in the *R* image some distortion is seen. The $B-R$ image clearly shows the off-center dust lane along a position angle of about 140° which is not along either the major or the minor axis of the galaxy (see also the photographic picture by Barbon, Capaccioli, and Rampazzo 1982). However, the isophotes in the outer region are almost elliptical, so that if one looked at an overexposed picture, one would consider it a normal galaxy. Ionized gas was also detected in this galaxy. It appears that the ionized gas is distributed asymmetrically around the center; the line emission is weaker toward the location of the dust lane than that in the other side. At the position of the dust lane, the apparent $E(B-R)$ is 0.24 mag. Because of the fact that the obscuring dust may not reside in front of stars along the line of sight, the actual absorption of the line emission may be more

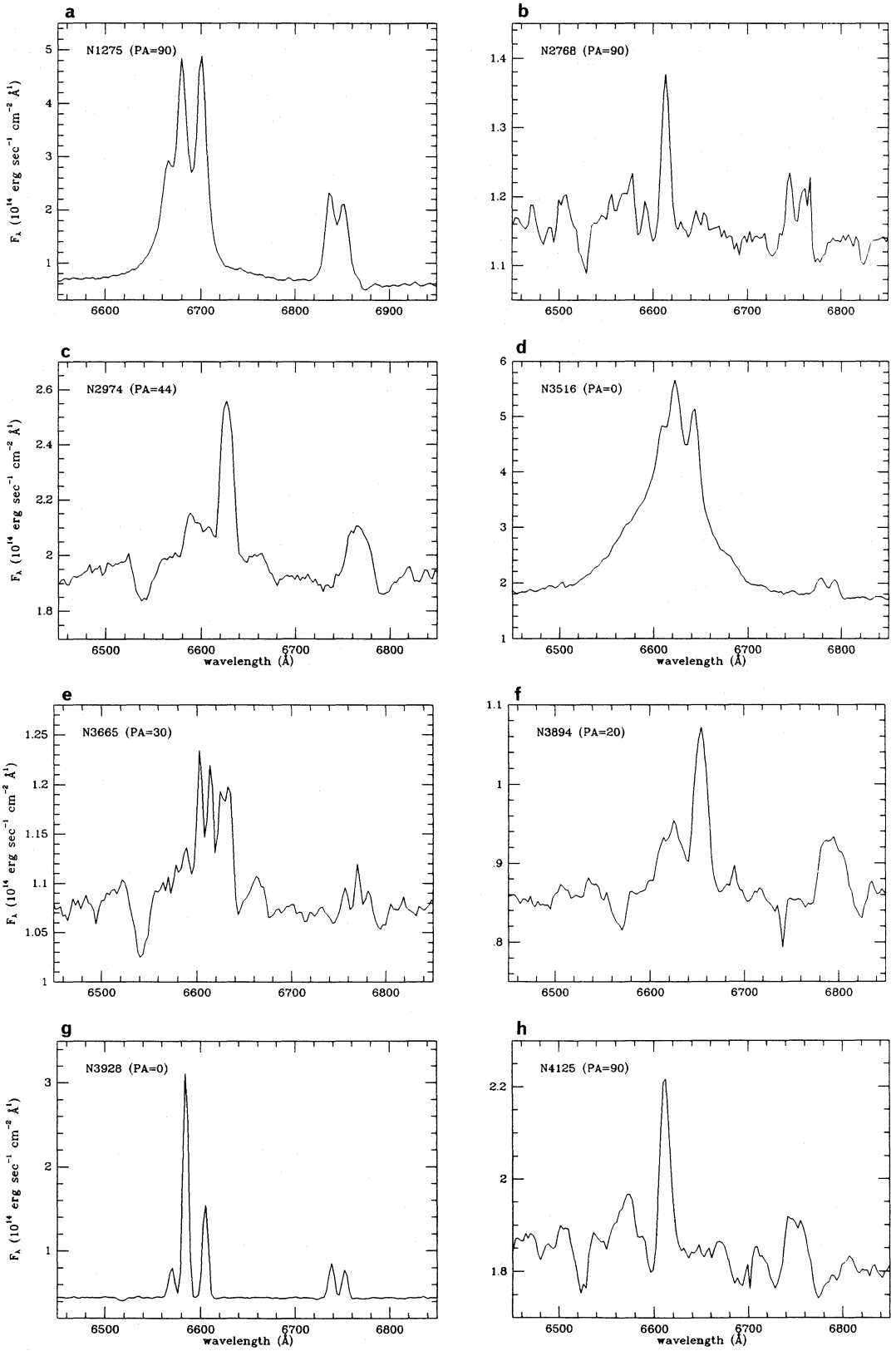

FIG. 16.—Optical spectra of (*a*) NGC 1275 at a position angle of 90°, (*b*) NGC 2768 at a position angle of 90°, (*c*) NGC 2974 at a position angle of 44°, (*d*) NGC 3516 at a position angle of 0°, (*e*) NGC 3665 at a position angle of 30°, (*f*) NGC 3894 at a position angle of 20°, (*g*) NGC 3928 at a position angle of 0°, (*h*) NGC 4125 at a position angle of 90°, (*i*) NGC 4261 at a position angle of 150°, (*j*) NGC 4374 at a position angle of 90°, (*k*) NGC 4589 at a position angle of 5°, and (*l*) of NGC 5273 at a position angle of 90°. The fluxes are in units of ergs s^{-1} cm^{-2} $Å^{-1}$. Hα, [N II] λ6548, [N II] λ6584, [S II] λ6713, and [S II] λ6737 lines are shown. The wavelength is the observed one, not corrected for the redshift.

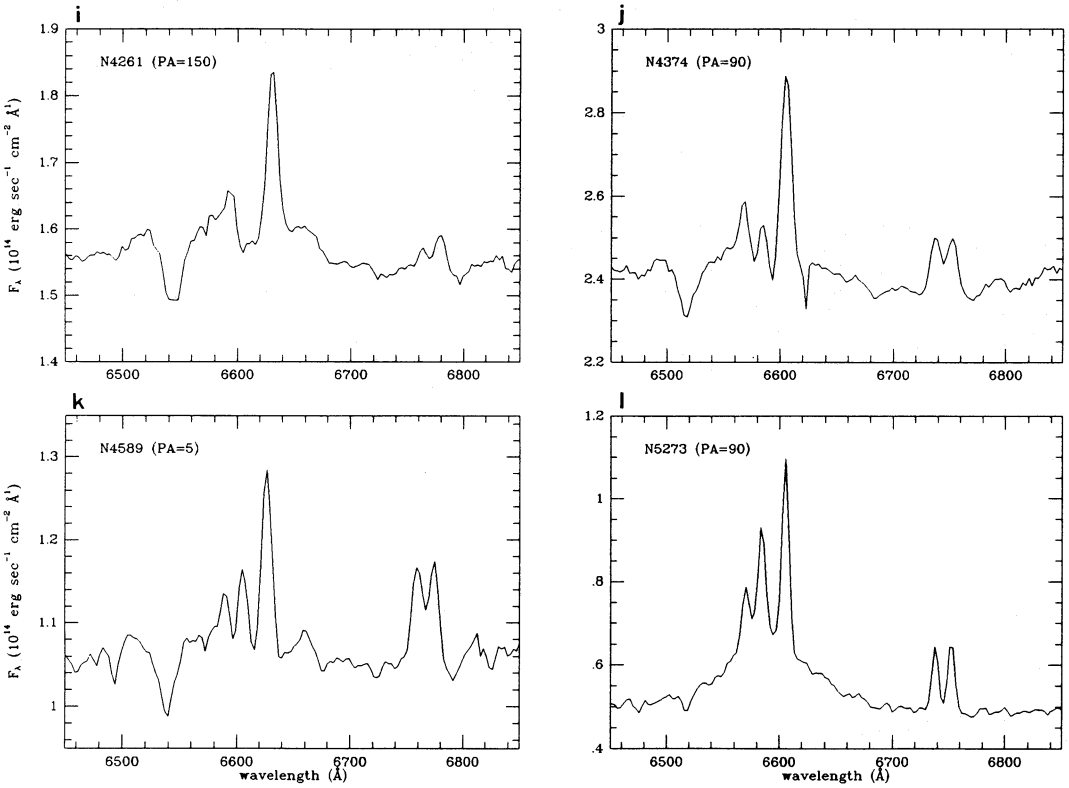

FIG. 16—*Continued*

significant than the observed. Without correcting dust absorption, our estimated total flux of Hα and [N II] lines is 1.5×10^{-13} ergs s^{-1} cm^{-2}, which is consistent with 1.7×10^{-13} ergs s^{-1} cm^{-2} measured by Keel (1983). If the ionized gas is actually distributed symmetrically around the center, the total flux would be about twice of the above value.

b) NGC 1052

The dust lane in NGC 1052 is well known (Gallagher 1986; Sparks *et al.* 1985). Comparing the *B* and *R* images, distortion in isophote contours in the *B* image is seen at PA = 35°, roughly along the minor axis. Isophote twisting in the *B* image also differs from that in the *R* image within 8″ of the center. The dust lane is distributed toward the east and toward the south from the center in a scale of 15″. In NGC 1052, the H I 21 cm line observation by van Gorkom *et al.* (1986) showed extended H I gas along the minor axis. The H I gas seems to be in continuation of the dust lane seen in the $B-R$ image.

Subtracting the continuum from the line image shows ionized gas in the central 10″ region. The ionized gas appears to be distributed similarly as the dust lane seen in $B-R$. The total line flux (Hα λ6563 + [N II] λ6548 + [N II] λ6584) is 8.1×10^{-13} ergs s^{-1} cm^{-2}. This value is consistent with 4.8×10^{-13} ergs s^{-1} cm^{-2} estimated by Fosbury *et al.* (1978), because the scanner aperture they used was only 1″.8 × 4″.5. Davies and Illingworth (1986) estimated a position angle of the rotation axis of the ionized gas, ~40°, which is consistent with the distribution of the ionized gas. The decoupled kinematics

TABLE 6

SPECTROSCOPIC DATA

Name	V_p (line) (km s^{-1})	V_*	V_r[a]	r (kpc)	i	V_r(corrected)[b]	$M(<r)$ ($M_\odot$)
N2768.....	1384:	1363	140	5″(0.44)	...	...	$>2.0 \times 10^9$
N2974.....	1958:	1924	265	12 (1.31)	54°	330	3.3×10^{10}
N3516.....	2696:	2602	180	4 (0.60)	...	...	$>4.5 \times 10^9$
N3665.....	2061	2080	285	10 (1.28)	46	395	4.6×10^{10}
N3894.....	3165	3259	275:	3 (0.54)	57	328	1.3×10^{10}
N3928.....	914	990	0	...	...	...	...
N4125.....	1293	1340	230	15 (1.37)	67	250	2.0×10^{10}
N4261.....	2172	2227	75	2 (0.13)	...	...	$>1.7 \times 10^8$
N4374.....	993	1033	130	12 (0.79)	62	150	4.1×10^9
N4589.....	1935	1971	170	9 (1.08)	63	190	9.0×10^9
N5273.....	960	1089	0	...	...	...	...

[a] Observed rotation velocity at the radius r.
[b] Rotation velocity corrected for the inclination i.

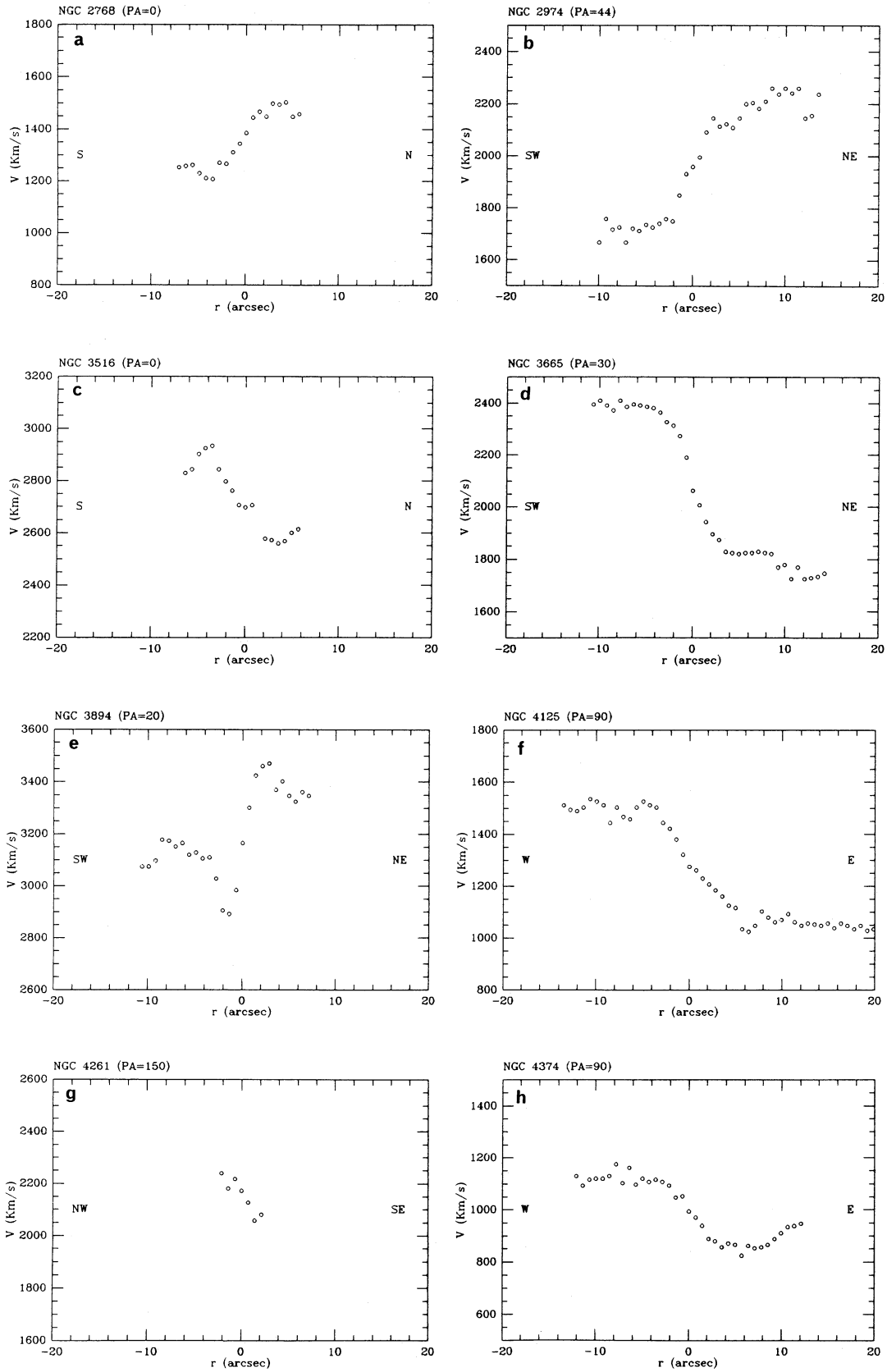

FIG. 17.—Rotation curves determined by the emission lines (Hα or [N II] λ6584) for (*a*) NGC 2768 at a position angle of 0°, (*b*) NGC 2974 at a position angle of 44°, (*c*) NGC 3516 at a position angle of 0°, (*d*) NGC 3665 at a position angle of 30°, (*e*) NGC 3894 at a position angle of 20°, (*f*) NGC 4125 at a position angle of 90°, (*g*) NGC 4261 at a position angle of 150°, (*h*) NGC 4374 at a position angle of 90°, and (*i*) NGC 4589 at a position angle of 5°.

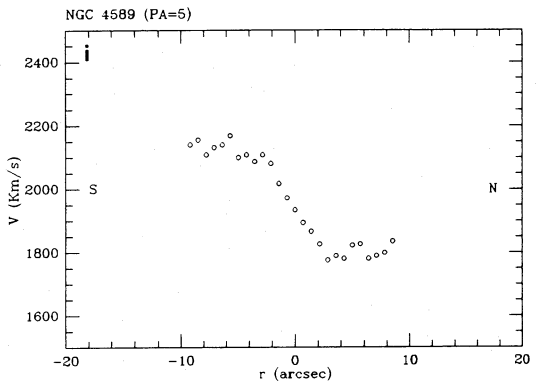

FIG. 17—*Continued*

of the gas and stellar systems (Davies and Illingworth 1986) favors an external origin of the interstellar matter. NGC 1052 has a nearby (15′ to the southwest of the galaxy) spiral galaxy, NGC 1042, which might have supplied NGC 1052 with interstellar matter. The tidal tail of H I gas is seen to the southwest of the galaxy (van Gorkom *et al.* 1986).

c) NGC 1275

NGC 1275 is known to have strong emission lines and it is identified as a Seyfert galaxy (e.g., Weedman 1977). The ionized gas in NGC 1275 is very distinctly distributed; a strong central source and various filament-like features are seen. Our total measured emission line flux (Hα and [N II] λ6584) is 3.2×10^{-12} ergs s^{-1} cm^{-2} and the Hα flux is 1.5×10^{-12} ergs s^{-1} cm^{-2}. These results are consistent with the Hα + [N II] λ6584 line flux of 2.8×10^{-12} ergs s^{-1} cm^{-2} measured within an aperture of radius 28″ (Heckman 1981), and also with the Hβ flux of 3.5×10^{-13} ergs s^{-1} cm^{-2} within 25″ diameter (Wirth, Kenyon, and Hunter 1983) if the ratio of Hα and Hβ flux is about 3 (Kent and Sargent 1979). But it is about a factor of 2 smaller than the estimation of Hα flux, 3.3×10^{-12} ergs s^{-1} cm^{-2} by Cowie *et al.* (1983), who used a larger field of view (4′.5) than ours (about 1′). The estimated mass of the ionized gas is 1.2×10^6 $M_\odot$ which is the largest in our sample. The presence of a dust lane is not clear because the *R* image is significantly affected by the strong emission lines, and because foreground Galactic stars near the center of the *B*−*R* image make it very difficult to detect a dust lane. However, the strong far-infrared emission and the detection of CO molecular material (Lazareff *et al.* 1989) indicate the presence of cold interstellar gas in this galaxy.

d) NGC 2768

NGC 2768 is an example with a dust lane along the minor axis. The distortion of isophotes is clearly seen along PA = 10°–20° in the *B* image and less distinctly in the *R* image. The *B*−*R* image shows dust distributed roughly along the minor axis which looks like a single-sided jet. It may be due to a projection effect that dust on the far side is not seen easily.

Ionized gas is concentrated rather symmetrically in the central core. From the emission line, rotation along a position angle of 0° (close to the minor axis) is seen within 7″, but within the uncertainty, no rotation is detected at a position angle of 90°. The sense of rotation is consistent with the distribution of the dust. The line emission may be absorbed in the direction of the dust. The velocity field is symmetric around the center, indicating a rotating gas disk. The velocity increases outward to 4″ and then decreases. The rotation velocity measured at 5″ (440 pc at a distance of 18.1 Mpc) is 140 km s^{-1}. Since it is doubtful that this galaxy is oblate and emission lines are probably absorbed by dust, correction for projection is not easy. We estimate, neglecting the inclination, a total mass $2 \times 10^9/\cos(i)$ $M_\odot$ within 5″ (see Table 6). The Hα line is very weak relative to the [N II] line [the ratio of *F*([N II]) to *F*(Hα) is 2.8]—typical for a LINER galaxy. The estimated mass of the ionized gas is about 2×10^3 $M_\odot$. Major axis rotation of the stellar system has been reported (Illingworth 1977), and therefore the gas and stellar system have different kinematics, which may be explained by an external origin of the gas.

e) NGC 2974

NGC 2974 is a typical example with a dust lane along the major axis. The H I data (Kim *et al.* 1988) and kinematics of the ionized gas also confirm the coupling of the interstellar gas and the stellar kinematics. Like most galaxies with major axis dust lanes, there is no clear distortion in isophotes in the *B* and *R* images, but ellipticity in the *B* and *R* images differs such that the contour in the *R* image is flatter than that in the *B* image and the *B*−*R* image shows dust lane along the major axis of the galaxy. A different degree of isophote twisting in the *B* and *R* images is also seen in the inner 10″ region. The H I 21 cm line was detected in NGC 2974, and the distribution of the H I gas is extended along the major axis to 3′ (Kim *et al.* 1988).

The ionized gas is distributed roughly along the major axis (see also Demoulin-Ulrich, Butcher, and Boksenberg 1984). The rotation of the ionized gas is seen along the major axis, consistent with the distribution of the gas and dust. The velocity field is symmetric around the center, and the velocity rapidly increases within 5″ and stays at a nearly constant value outward. The rotation velocity at 12″ is 265 km s^{-1}, which agrees with the rotation velocity determined by the H I λ21 cm line observation. Correcting for projection according to the relative axial ratio of the ionized gas distribution (inclination of gas = 54°), and assuming circular rotation, we estimate the mass within 12″ of 3.2×10^{10} $M_\odot$. The relative line ratios are similar to those for NGC 2768—Hα is weaker than [N II] [the ratio of *F*([N II] to *F*(Hα) is 2.7]. The estimated mass of ionized gas is about 1.1×10^4 $M_\odot$. The well-aligned kinematics of the gas and stars and the lack of a nearby gas-rich companion is not in accord with the idea of external acquisition of interstellar gas in NGC 2974 (for details see Kim *et al.* 1988).

f) NGC 3415

Although NGC 3415 is identified as E5 in RSA and S0+ in RC2, it has a quite abnormal light distribution as seen in Figure 13. (In the figure, the vertical strip to the right of the galaxy is columns saturated by a nearby bright star.) Isophote twisting and irregular distortions are seen in all images, most significantly in the line image. A tightly wound spiral-like structure (Fig. 12) is clearly seen in the Hα image in a scale of 20″ (3.6 kpc in a distance of 37.4 Mpc). Note that the outer envelope is almost elliptical. Enhanced star formation seems to cause the observed deviation from the simple elliptical shape.

g) NGC 3516

Like NGC 3415, NGC 3516 has a spiral-like structure in the Hα image (Fig. 12). In Figure 14, the images in all bands are shown. In the outer envelope, the isophotes look elliptical with a position angle of the major axis −5°. In the intermediate region (8″–12″ from the center), deviation of isophotes from

elliptical shapes is seen; there seems to be a stellar disk at a position angle of $-15°$. And in the inner region, the position angle of the major axis is shifted in the opposite direction (PA = $\sim 50°$). The strange-looking light distribution is most clearly seen in the line image. After continuum subtraction, the spiral-shaped structure is seen in Figure 12—less tightly wound than that of NGC 3415.

NGC 3516 has a very broad component in its Hα emission line, as already noted (Weedman 1977; Filippenko and Sargent 1985). The line profile is too broad to fit in a single narrow-band filter. We used two adjacent filters to estimate the line flux. Estimated total line flux is 2.4×10^{-12} ergs s^{-1} cm^{-2}. The broad-line component is seen only in the center (within 2″), and outside the broad-line region, each line (Hα and [N II]) is resolved. Although the nuclear component dominates in the center, the line ratio off nucleus is consistent with current star formation (Hα is stronger than [N II]). Gas rotation is measured within 7″. The profile of velocity field is similar to that in NGC 2768—the rotation velocity reaches its maximum and then decreases out to the observation limit. The estimated mass of the ionized gas, using an electron density of 1000 cm^{-3}, is about $4 \times 10^5\ M_\odot$ which is larger than the typical mass (10^3–$10^4\ M_\odot$) in early-type galaxies.

h) NGC 3665

A very strong obscuring dust band is seen in all passbands. The dust lane, which is at PA = 25°, lies nearly along the major axis but is off-center to the northwest of the center. The $B-R$ image shows the dust lane as well as a red nucleus; it may be interpreted as a ring and the far side of the dust is not seen. Ionized gas is also distributed along the major axis through the center, and at the position of the dust lane the emission line seems to be strongly attenuated; the contour is steeper toward the direction of the dust lane, and apparently no emission is seen at the position of the dust band. The line profile taken through the center shows double peaks in both Hα and [N II] line, most probably due to the strong dust absorption. The rotation centered about the nucleus is measured out to 15″. The sense of rotation along the major axis is consistent with the distribution of the gas and dust. Like NGC 2974, the rotation velocity increases rapidly within 4″ and reaches a constant value. The measured rotation velocity is 285 km s^{-1} at 10″. Assuming that the line emission from the northwest side is absorbed by the strong dust lane, we estimate that the inclination of the gas disk is 46°, and further assuming circular rotation, we estimate that the mass within 10″ is $4.6 \times 10^{10}\ M_\odot$.

i) NGC 3894

Like NGC 2974, the dust lane and ionized gas are seen along the major axis of the galaxy, and the gas rotates along the major axis. However, the gas kinematics is rather peculiar—in the central few arcsec, the rotation velocity increases very rapidly, suddenly decreases, and then reaches roughly a constant velocity. The gas in this galaxy does not seem to be in a circularly rotating disk. Therefore, the measured rotation velocity is uncertain. In Table 6, the maximum velocity, 275 km s^{-1} at 3″ is given, and the estimated mass is approximately $10^{10}\ M_\odot$ within 3″ after correcting for the 57° inclination angle. Also the VLBI radio axis (Wrobel, Jones, and Shaffer 1985) is almost perpendicular to the direction of the dust lane.

j) NGC 3928

Van den Bergh (1980) found a tightly wound spiral structure in the center surrounded by a featureless bulge (see also Taniguchi and Watanabe 1987). In Figure 14, the images in four bands are shown. The B and line images show distorted isophotes. In the line image after continuum subtraction (Fig. 12), several discrete sources of the emission lines are seen, roughly forming a spiral structure. Double peaks are seen at the center with the strongest source located within 3″ north of the center. Where the emission line is seen, the emission in B is strong relative to that in R, particularly to the west and to the north of the center. It suggests the presence of young stars. The line ratio is also consistent with the view that the ionization is caused by the stellar radiation as in a Galactic H II region because Hα is stronger than [N II]. NGC 3928 has strong lines, but no rotation is seen along the major or minor axis, probably because the gas is in a face-on distribution.

k) NGC 4125

Like NGC 2974, the distribution and kinematics of the gas and dust are similar to that of the stellar system. Both the dust lane and ionized gas are distributed along the major axis and rotation is seen along this axis. The rotation velocity profile is also similar to that of NGC 2974. The measured rotation velocity is 230 km s^{-1} at 15″. Correcting projection according to the relative axial ratio of the ionized gas distribution (inclination of gas = 67°), and assuming circular rotation, we estimate that the mass within 15″ is $2.0 \times 10^{10}\ M_\odot$. In NGC 4125, a slow rotation along the minor axis in addition to the faster rotation along the major axis has been determined from stellar absorption line observations (Bertola *et al.* 1984); this can be evidence of triaxiality. Along the minor axis, we could barely see the gas rotation, although it is subject to a quite large uncertainty. The gas rotation velocity along the minor axis is about 50 km s^{-1} which is about the detection limit.

l) NGC 4261

NGC 4261 has boxy isophotes rather than an ellipse (see also Lauer 1985). Both the B and R isophotes apparently show no distortion and twisting; however, ellipticities are different between the two images. The contours in the R image are flatter than those in the B image, and the $B-R$ image therefore shows a dust lane elongated along the major axis. NGC 4261 is unique in the sense that the angular momentum vector of the stellar rotation is parallel to the apparent major axis, suggesting a prolate or triaxial nature for a galaxy figure (Davies and Birkinshaw 1986). Also Mollenhoff and Bender (1987) reported a central dust lane at PA = 355° whose distribution is parallel to the stellar rotation axis, suggesting a triaxial galaxy. We confirm the distribution of the dust lane along the major axis, and the gas rotation is also seen along the major axis although the gas is so centrally concentrated that the observed velocity gradient is just above the detection limit. The measured rotation velocity at 2″ is about 75 km s^{-1} without inclination correction. Interestingly, the dust distribution is perpendicular to the radio axis of PA = 88° (Birkinshaw and Davies 1985).

m) NGC 4374

Distortion of isophotes in the B image is clearly seen at a position angle of about 90°. As Hansen, Norgaard-Nielson, and Jorgenson (1985) found, the dust lane is distributed along the east-west direction, which does not match either the major or minor axis of the stellar system but is perpendicular to the distribution of radio continuum (Kotanyi and Ekers 1979). The ionized gas is distributed very similarly to the dust, and the gas rotation is consistent with a flattened gas and dust distribution. The velocity field is slightly asymmetric; in the east the velocity

falls off outside of 7″, but in the west it remains constant. The measured rotation velocity is 130 km s^{-1} at 12″. Correcting projection according to the axial ratio of the ionized gas distribution (inclination of gas = 62°), and further assuming circular rotation, which may not be valid due to the asymmetry in the rotation curve, we approximately estimate the mass within 12″ of $4.1 \times 10^9 M_\odot$.

n) NGC 4589

NGC 4589 is another example with a minor axis dust lane like NGC 2768—a candidate for having a triaxial figure. In this galaxy, both the dust and ionized gas are aligned along the minor axis, more or less symmetrically around the center. Minor axis rotation of the stellar system as well as major axis rotation was reported in this galaxy (Wagner, Bender, and Mollenhoff 1988), suggesting a triaxial figure. Gas rotation is also seen along the minor axis. The measured rotation velocity is 170 km s^{-1} at 9″. Correcting projection according to the axial ratio of the ionized gas distribution (inclination of gas = 63°), and assuming circular rotation, we estimate the mass within 9″ of $9.0 \times 10^9 M_\odot$.

o) NGC 5018

The isophote in the *B* image is rather irregular. A dust lane is seen to the northwest of the center, and a ripple and shell are seen on a larger scale (Schweizer and Ford 1985). From H I observations, several blobs of H I sources were seen within a few arcmin of the center (see Kim *et al.* 1988). These H I sources may correspond to the dust ripples seen in the optical. However, for a clear correlation of the H I and optical image, better H I observations are needed. The optical emission lines in NGC 5018 are marginally detected in our spectrum; absorption is seen adjacent to the line so that it is hard to determine the line emission. Detection in the [O II] line was reported at about the 2 σ level (Caldwell 1984). In the center of NGC 5018 there are double sources of radio continuum (Kim *et al.* 1988), one in the center and another at about 1′ east of the center. However, no off-center counterpart is seen in the optical images.

p) NGC 5273

Irregular distortion is seen in the *B* image. The $B-R$ image reveals that the dust is distributed only in the east half of the galaxy. Ionized gas is seen only in the central core, and no rotation is found from the emission lines along the major and minor axes. NGC 5273 has a broad Hα component and it is a known Seyfert galaxy (Filippenko and Sargent 1985).

V. DISCUSSION

We detect dust lanes and ionized gas in more than half of the sample studied. Distribution of the dust and gas seems to indicate that the interstellar matter in an early-type galaxy is often in the form of a disk rotating around the center of the galaxy. Kinematics of the ionized gas confirms the observed distribution of the gas and dust seen in the direct imaging. Further, the usual symmetry in the rotation curve around the center is consistent with circular orbits in a rotating disk.

Two galaxies in our sample have been mapped in the H I λ21 cm line; NGC 1052 (van Gorkom *et al.* 1986) and NGC 2974 (Kim *et al.* 1988). In both galaxies the orientations of dust lanes and H I are the same, although the H I line emission is extended out to the optical radius while the dust lane is concentrated in the central part. It is likely that the extended H I gas seen in the λ21 cm line is in continuation of the more compact dust lane seen optically, because the method using the optical $B-R$ color excess is not sensitive to the outer region.

The detection rate of dust lanes and ionized gas in our sample is a little bit higher than previous estimates (see Sadler and Gerhard 1986). This is not surprising because the galaxies are selected by the infrared fluxes. The analysis of the *IRAS* data shows that galaxies with dust lanes and/or H I gas are very often sources of far infrared emission (Kim 1988). It implies that the dust lanes seen in the optical images are responsible for the far-infrared emission.

There are at least two possible explanations for an origin of interstellar matter: accumulation of mass loss from evolved giant stars, namely an internal origin; and mass from outside sources, namely an external origin (Raimond *et al.* 1981; Knapp, Turner, and Cuniffe 1985; Kim *et al.* 1988). The H I observations of two galaxies, NGC 2974 and NGC 5018, which are in distinct environments, showed that neither possibility can be ruled out for an origin of cold interstellar matter (Kim *et al.* 1988). NGC 2974 is an isolated galaxy within a 1° by 1° field and has a very regular distribution and kinematics of H I gas. The H I gas in this galaxy is therefore most easily explained by an internal origin, i.e., by stellar sources. The optical observations for NGC 2974, NGC 3894, and NGC 4125 also revealed that the gas distribution and kinematics of these galaxies are aligned with the stellar systems.

On the contrary, NGC 1052 (van Gorkom *et al.* 1986) and NGC 4278 (Raimond *et al.* 1981) have H I gas kinematics decoupled from that of the stellar system, and they have nearby companions which might have supplied gas to these galaxies. Particularly, in the NGC 5018 and NGC 5022 pair (Kim *et al.* 1988), gas currently being transferred from the gas-rich spiral (NGC 5022) to the elliptical (NGC 5018) was seen in the H I observation. The optical imaging provides further evidence for decoupled kinematics of gas and stars. Particularly NGC 1052, NGC 2768, and NGC 4261 have gas whose kinematics are not aligned with the stellar kinematics. Therefore, we cannot single out an origin for the cold interstellar gas, and the relative importance of the internal and external sources seems to vary from one galaxy to another, depending on, for example, the environment of the galaxy.

The dynamical structure of early-type galaxies is not as simple as the picture of a rotating oblate spheroid (see Binney 1982). In addition to slow rotation of stellar systems (Bertola and Capaccioli 1975; Illingworth 1977) and isophote twisting, the failure of the simple model is seen from the presence of minor axis dust lanes. Many galaxies in our sample show such features which cannot be explained by an oblate figure, although some ellipticals may be purely isotropic oblate rotators (see Nieto, Capaccioli, and Held 1988). While NGC 2974, NGC 3894, NGC 4125, and NGC 4261 have dust and gas distributions which follow the stellar system, we found dust lanes which are not aligned with the major axis of the stellar system in NGC 404, NGC 1052, NGC 2768, NGC 4374, and NGC 4589. Long-slit spectroscopy confirms the misalignment—the gas kinematics is different from the stellar kinematics in these galaxies. Unless these are transient phenomena on the way to settlement in equilibrium planes, they are evidence of triaxial nature of a galaxy figure. In a triaxial stellar system, stable orbits exist in the planes perpendicular to the short and long axes (Schwarzschild 1979; van Albada, Kotanyi, and Schwarzschild 1982). The stellar rotation along the minor axis was found in NGC 4125 (Bertola *et al.* 1984)

and NGC 4261 (Davies and Birkinshaw 1986), which suggests these galaxies are also triaxial or prolate. No rotation along the apparent minor axis is expected in an oblate figure, since the apparent major axis is the same as the physical major axis in this figure.

Using the gas rotation, we can measure the mass inside a given radius. To measure a mass-to-light ratio, we estimate the luminosity within a radius, using the empirical $r^{1/4}$ law, because it fits well the observed light distribution in our sample and because it is convenient (see Kormendy 1977). By fitting the B image into concentric ellipses, the light distribution averaged on the ellipse is measured along the radius at 45° from the major axis. The effective radius is then measured by fitting the light curve to the $r^{1/4}$ law. The estimated effective radius is given in Table 7. Using the table in Young (1976), we measure the luminosity within the radius. The estimated mass-to-light ratio (M/L_B in solar units) is given in Table 7. The mass-to-light ratios range from a few to about 10. The observed range is partly because the rotation velocities were estimated at different radii. For NGC 3894, the rotation curve is very abnormal and the rotation velocity is hard to measure accurately. Consequently the error on this velocity is large. In NGC 2786 and NGC 4261, ionized gas is detected only in the center and hence the inclination correction might increase the rotation velocity.

The existence of dark matter is not yet clearly determined in early-type galaxies even though it is well known in the outer regions of spiral galaxies (see, for example, Faber and Gallagher 1979). In our sample, it appears that the mass-to-light ratio in the center is smaller than that in the outer part. In the rising portion of the rotation curve, the velocity gradient is too steep to be matched with a constant mass-to-light ratio. For example, NGC 2768 has M/L_B of 3.2 at 2″ and 4.8 at 5″. NGC 2974 has M/L_B of 5.5 at 3″ and 9.7 at 12″. From the H I data of NGC 2974 (Kim *et al.* 1988), M/L_B becomes 24 at 2′. The variation of the mass-to-light ratio has been reported in NGC 7097 (Caldwell, Kirshner, and Richstone 1986) and NGC 5898 (Bertola and Bettoni 1988). This result strongly suggests the existence of dark matter in early-type galaxies, as in spiral galaxies.

Kotanyi and Ekers (1979) reported a relationship between relative orientations of the dust lane and the radio axis for several strong radio galaxies with dust lanes, suggesting that the radio jet might be confined by the surrounding gas. In our dust lane galaxies, NGC 1052 (Jones, Wrobel, and Shaffer 1984; Wrobel 1984), NGC 3665 (Birkinshaw and Davies 1985), NGC 3894 (Wrobel, Jones, and Shaffer 1985), NGC 4261 (Birkinshaw and Davies 1985) and NGC 4374 (Jones, Sramek, and Terzian 1981*a*, *b*) have known radio distributions. In NGC 3665, NGC 3894, NGC 4261, and NGC 4374, the dust lanes are indeed almost perpendicular to the direction of the radio jets, indicating the interstellar matter may confine the radio jets. Also Wrobel, Jones, and Shaffer (1985) noted a morphological difference in NGC 3894 between the parsec scale and tens of kiloparsec scale structures which might be caused by the interaction with the interstellar matter. In NGC 1052, the position angle of the VLBI source is 63° and the position angle of the VLA source is about 95° (Wrobel 1984; Jones, Wrobel, and Shaffer 1984). Neither of them is perpendicular to the distribution of the dust and gas. However, the perpendicular relationship is still possible, if the galaxy is triaxial as suggested by the distribution and kinematics of the interstellar matter (see also Davies and Illingworth 1986).

TABLE 7

MASS-TO-LIGHT RATIO

Name	V_r (corrected) (km s^{-1})	r (kpc)	$M(<r)$ ($M_\odot$)	r_e	M/L_B ($M_\odot/L_\odot$)
N2768.....	140[a]	0.44	$>2.0 \times 10^9$	88″	>4.8
N2974.....	330	1.31	3.3×10^{10}	32	9.7
N3894.....	328	0.54	1.3×10^{10}	23	14.2
N4125.....	250	1.37	2.0×10^{10}	57	4.8
N4261.....	75[a]	0.13	$>1.7 \times 10^8$	23	>0.54
N4374.....	150	0.79	4.1×10^9	55	1.7
N4589.....	190	1.08	9.0×10^9	31	2.7

[a] No correction for inclination is applied.

Since a few emission line galaxies in the sample have been detected in X-rays (Forman, Jones, and Tucker 1985; Canizares, Fabbiano, and Trinchieri 1987), we can test the hypothesis made for the center of cluster of galaxies that optical line emissions result from recombinations out of the X-ray cooling flow (see Cowie *et al.* 1983). Equating the cooling rate and X-ray luminosity and assuming that each recombing proton produces one Hα photon (Cowie *et al.* 1983), we get the following relation between Hα luminosity and X-ray luminosity,

$$L(\mathrm{H}\alpha) = 7.3 \times 10^{-4}\left(\frac{\mu}{0.5}\right)\left(\frac{10^7}{T}\right)L_x \, .$$

For the three galaxies, NGC 2974, NGC 4374, and NGC 4589, which have been detected both at optical line and X-ray, the X-ray flux is at least two orders of magnitude smaller than that expected in the above relation. Therefore, H II gas (and probably H I gas) cannot originate from the X-ray cooling flow in individual early-type galaxies, although this may be the case in clusters of galaxies. A different origin for hot and cold gas is also supported by the finding that the gas kinematics is often different from the stellar kinematics in early-type galaxies.

Although the observed ionized gas does not result from the recombination out of the cooling flow, X-ray radiation from the hot gas may in part contribute to ionize the interstellar gas. To see its contribution, we estimate the number of ionizing photons by integrating, from X-rays to 912 Å, the spectrum which is assumed to be bremsstrahlung emission at temperature 10^7 K. For the three galaxies which have been observed in X-rays, the estimated number of ionizing photons from the hot gas is about 5%–10% of that required for the observed line fluxes.

Some early-type galaxies do have excess ultraviolet emissions which may be attributed to young star formation (Burstein *et al.* 1988). If the ionized gas seen in the optical emission lines is by the young OB stars, there will be a relationship between the excess UV light and the emission line intensity. A subset of our sample, NGC 1052, NGC 4125, and NGC 4374, has been observed in the UV by Burstein *et al.* (1988). The excess UV light at 1550 Å, which is possibly from the young stars, is calculated by subtracting the spectra of NGC 3379 after corrected for the galactic extinction. The energy distribution of NGC 3379 is used as a template which represents the cool population. It is not clear how to extrapolate the observed energy distribution to below 912 Å. Simply assuming that the excess light is from stars with $T = 40{,}000$ K, typical for O6 stars, we calculate the ratio of the number of ionizing photons to the energy at 1550 Å, 4.4×10^{13} cm^{-2} s^{-1} (ergs s^{-1} cm^{-2} Å^{-1})$^{-1}$. From recombination theory (see Osterbrock 1974), about 8.6 recombinations produce one Hβ

TABLE 8

COMPARISON OF EXCESS UV LIGHT AND LINE EMISSION

Name	$F_\lambda(1550\ \text{Å})_{\text{excess}}$ (ergs s^{-1} cm^{-2} Å^{-1})	$F(\text{H}\alpha)_{\text{expected}}$ (ergs s^{-1} cm^{-2})	$F(\text{H}\alpha)_{\text{observed}}$ (ergs s^{-1} cm^{-2})
NGC 1052.....	1.3×10^{-15}	8.4×10^{-14}	3.9×10^{-13}
NGC 4125.....	1.6×10^{-16}	1.0×10^{-14}	3.6×10^{-14}
NGC 4374.....	7.5×10^{-16}	4.8×10^{-14}	5.1×10^{-14}

photon. The calculated Hα flux from the excess UV light, assuming $F(\text{H}\alpha) = 3 \times F(\text{H}\beta)$, and the observed flux are compared in Table 8. In NGC 1052 and NGC 4125, the observed Hα flux is larger than expected by a factor of 4 and in NGC 4374, the observed flux is comparable. Since the assumed energy distribution may even overestimate the ionizing flux, it seems that the observed UV excess does not provide enough ionizing photons to explain the line emission.

The observed intensity ratios of Hα to [N II] line also disagrees with ionization by the stellar radiation, and resemble that observed in LINER-type galaxies. Therefore, the ionization is most likely due to nuclear activity. The extent of the line emission may be useful to constrain a model; whatever the ionization mechanism is, the model should explain the extended line emission. Because the emission lines are extended (10″–20″), but not concentrated in the center, if the ionization is due to the photoionization by the power-law spectrum from the center, the radiation would have to penetrate a large distance (a few kpc).

Morphological types in early-type galaxies are often misidentified partly because of lacking proper photometric data and partly because of using overexposed photographic plates. Recent observations with high sensitivity and high dynamic range using the CCD detector revealed various such cases (see, for example, Ebneter and Balick 1985). In our sample, three galaxies do show minispiral structure in their emission-line images: NGC 3415 (E5 in RSA and S0+ in RC2), NGC 3516 (SB0 in RSA and RC2) and NGC 3928 (E0 in RC2). In these galaxies, the deviation of isophotes from the elliptical shape is seen only in the central region and they look normal in the outer envelope.

VI. SUMMARY

1. Selecting 26 galaxies by the *IRAS* fluxes, we detect dust lanes and ionized gas in more than half of them, proving that the far-infrared emission is a good indicator for the presence of interstellar matter.

2. Dust lanes and ionized gas are distributed in various ways—along the apparent major axis, minor axis, or a skewed axis. In general, triaxiality is required for a galaxy figure. The most probable candidates for triaxial galaxies are NGC 404, NGC 1052, NGC 2768, NGC 4261, NGC 4374, and NGC 4589.

3. The distributions of gas and dust and the rotation curves of the ionized gas are roughly symmetric about the center in most galaxies observed. The gas and dust seem to be in a circularly rotating disk.

4. The frequent misalignment of gas and stellar kinematic axes prefers an external origin for the cold interstellar matter. External acquisition of interstellar gas is favored particularly in NGC 1052, NGC 2768, NGC 4261, and NGC 5018.

5. The rotation curves determined from emission lines suggest the existence of dark matter in early-type galaxies as well as in spiral galaxies.

6. Ionized gas in early type galaxies (typical mass of 10^3–$10^4\ M_\odot$) is very often accompanied by cold gas and dust, possibly implying a common origin for the cold and warm gas.

7. In most early-type galaxies, the ratio of Hα to [N II] line is not consistent with ionization by stellar radiation, but rather with a LINER-type galaxy. The X-ray emission and UV radiation recently observed are insufficient to explain the observed line flux.

8. Our optical observations are consistent with the model in which cold gas and dust stem partly, if not totally, from external sources and settle down in a rotating disk under the triaxial potential. Part of the cold gas is accreting onto the center, and the gas near the nucleus is ionized by nuclear activity.

This work is based on part of the author's Ph.D. thesis at UCLA. I would like to express a great appreciation to my advisor, Mike Jura. Also I thank Matt Malkan for useful suggestions and Mary-Beth Kaiser for reading the paper. I am indebted to the staffs of Lick Observatory for their support. This work has been partly supported by NASA.

REFERENCES

Baldwin, J. A., Phillips, M. M., and Terlevich, R. 1981, *Pub. A.S.P.*, **93**, 5.
Barbon, R., Capaccioli, M., and Rampazzo, R. 1982, *Astr. Ap.*, **115**, 388.
Bertola, F. 1987, in *IAU Symposium 127, Structure and Dynamics of Elliptical Galaxies*, ed. T. de Zeeuw (Dordrecht: Reidel), p. 135.
Bertola, F., and Bettoni, D. 1988, *Ap. J.*, **329**, 102.
Bertola, F., Bettoni, D., Rusconi, L., and Sedmak, G. 1984, *A.J.*, **89**, 356.
Bertola, F., and Capaccioli, M. 1975, *Ap. J.*, **200**, 439.
Binney, J. 1982, *Ann. Rev. Astr. Ap.*, **20**, 399.
Birkinshaw, M., and Davies, R. L. 1985, *Ap. J.*, **291**, 31.
Burstein, D., Bertola, F., Faber, S. M., and Lauer, T. R. 1988, *Ap. J.*, **328**, 440.
Caldwell, N. 1984, *Pub. A.S.P.*, **96**, 287.
Caldwell, N., Kirshner, R. P., and Richstone, D. O. 1986, *Ap. J.*, **305**, 136.
Canizares, C. R., Fabbiano, G., and Trinchieri, G. 1987, *Ap. J.*, **312**, 503.
Cowie, L. L., Hu, E. M., Jenkins, E. B., and York, D. G. 1983, *Ap. J.*, **272**, 29.
Davies, R. L., and Birkinshaw, M. 1986, *Ap. J. (Letters)*, **303**, L45.
Davies, R. L., and Illingworth, G. B. 1986, *Ap. J.*, **302**, 234.
Demoulin-Ulrich, M.-H., Butcher, H. R., and Boksenberg, A. 1984, *Ap. J.*, **285**, 527.
de Vaucouleurs, G., de Vaucouleurs, A., and Corwin, H. 1976, *Second Reference Catalogue of Bright Galaxies* (Austin: University of Texas) (RC2).
Disney, M. J., and Wall, J. V. 1977, *M.N.R.A.S.*, **179**, 235.
Djorgovski, S. 1985, *Pub. A.S.P.*, **97**, 1119.
Dressel, L. L., and Condon, J. J. 1978, *Ap. J. Suppl.*, **36**, 53.
Ebneter, K., and Balick, B. 1985, *A.J.*, **90**, 183.
Ebneter, K., Djorgovski, S., and Davis, M. 1988, *A.J.*, **95**, 422.
Faber, S. M., and Gallagher, J. S. 1979, *Ann. Rev. Astr. Ap.*, **17**, 135.
Filippenko, A. V., and Sargent, W. L. W. 1985, *Ap. J. Suppl.*, **57**, 503.
Ford, H. C., and Butcher, H. 1979, *Ap. J. Suppl.*, **41**, 147.
Forman, W., Jones, C., and Tucker, W. H. 1985, *Ap. J.*, **293**, 102.
Fosbury, R. A. E., Mebold, U., Goss, W. M., and Dopita, M. A. 1978, *M.N.R.A.S.*, **183**, 549.
Gallagher, J. S. 1986, *Pub. A.S.P.*, **98**, 81.
Hansen, L., Norgaard-Nielson, H. U., and Jorgenson, H. E. 1985, *Astr. Ap.*, **149**, 442.
Heckman, T. M. 1980, *Astr. Ap.*, **87**, 152.
———. 1981, *Ap. J. (Letters)*, **250**, L59.
Hummel, E. 1980, *Astr. Ap. Suppl.*, **41**, 151.
Illingworth, G. D. 1977, *Ap. J. (Letters)*, **218**, L43.
Jones, D. L., Sramek, R. A., and Terzian, Y. 1981*a*, *Ap. J.*, **276**, 480.
———. 1981*b*, *Ap. J. (Letters)*, **277**, L57.

Jones, D. L., Wrobel, J. M., and Shaffer, D. B. 1984, *Ap. J.*, **276**, 480.
Jura, M. 1986, *Ap. J.*, **306**, 483.
Jura, M., Kim, D. W., Knapp, G. R., and Guhathakurta, P. 1987, *Ap. J. (Letters)*, **312**, L11.
Keel, W. C. 1983, *Ap. J.*, **269**, 466.
———. 1985, in *Astrophysics of Active Galaxies and QSOs*, ed. J. S. Miller (Mill Valley: University Science Books), p. 1.
Kent, S. M., and Sargent, W. L. W. 1979, *Ap. J.*, **230**, 667.
Kim, D. W. 1988, Ph.D. thesis, UCLA.
Kim, D. W., Guhathakurta, P., van Gorkom, J. H., Jura, M., and Knapp, G. R. 1988, *Ap. J.*, **330**, 684.
Knapp, G. R., Guhathakurta, P., Kim, D. W., and Jura, M. 1989, *Ap. J. Suppl.*, **70**, 329.
Knapp, G. R., Turner, E. L., and Cunniffe, P. E. 1985, *A.J.*, **90**, 454.
Kormendy, J. 1977, *Ap. J.*, **218**, 333.
Kotanyi, C. G., and Ekers, R. D. 1979, *Astr. Ap.*, **73**, L1.
Lauer, T. R. 1985, *M.N.R.A.S.*, **216**, 429.
Lazareff, B., Lequeux, J., Kim, D.-W., and Jura, M. 1989, in preparation.
Merritt, D., and de Zeeuw, T. 1983, *Ap. J. (Letters)*, **267**, L19.
Mollenhoff, C., and Bender, R. 1987, *Astr. Ap.*, **174**, 63.
Nieto, J.-L., Capaccioli, M., and Held, E. V. 1988, *Astr. Ap.*, **195**, L1.
Oke, J. B. 1974, *Ap. J. Suppl.*, **27**, 21.
Osterbrock, D. E. 1974, *Astrophysics of Gaseous Nebulae* (San Francisco: Freeman and Co.), p. 71.
Phillips, M. M., Jenkins, C. R., Dopita, M. A., Sadler, E. M., and Binette, L. 1986, *A.J.*, **91**, 1062.
Pogge, R. W., and Eskridge, P. B. 1987, *A.J.*, **90**, 183.
Raimond, E., Faber, S. M., Gallagher, J. S., and Knapp, G. R. 1981, *Ap. J.*, **246**, 108.
Rees, M. J. 1984, *Ann. Rev. Astr. Ap.*, **22**, 471.
Sadler, E. M. 1987, in *IAU Symposium 127, Structure and Dynamics of Elliptical Galaxies*, ed. T. de Zeeuw (Dordrecht: Reidel), p. 125.
Sadler, E. M., and Gerhard, O. E. 1985, *M.N.R.A.S.*, **214**, 177.
Sandage, A. R., and Tammann, G. A. 1981, *Revised Shapley-Ames Catalogue of Galaxies* (Washington: Carnegie Institution of Washington) (RSA).
Schwarzschild, M. 1979, *Ap. J.*, **232**, 236.
Schweizer, F., and Ford, W. K. 1985, in *New Aspect of Galaxy Photometry*, ed. J.-L. Nieto (Berlin: Springer), p. 145.
Schweizer, F. 1987, in *IAU Symposium 127, Structure and Dynamics of Elliptical Galaxies*, ed. T. de Zeeuw (Dordrecht: Reidel), p. 109.
Sparks, W. B., *et al.* 1985, *M.N.R.A.S.*, **217**, 87.
Stone, R. P. S. 1977, *Ap. J.*, **218**, 767.
Taniguchi, Y., and Watanabe, M. 1987, *Ap. J.*, **313**, 89.
Tohline, J. E., Simonson, G. F., and Caldwell, N. 1982, *Ap. J.*, **252**, 92.
van Albada, T. S., Kotanyi, C. G., and Schwarzschild, M. 1982, *M.N.R.A.S.*, **198**, 303.
van den Bergh, S. 1980, *Pub. A.S.P.*, **92**, 409.
van Gorkom, J. H., *et al.* 1986, *A.J.*, **91**, 791.
Wagner, S. J., Bender, R., and Mollenhoff, C. 1988, *Astr. Ap.*, **195**, L5.
Wardle, M., and Knapp, G. R. 1986, *A.J.*, **91**, 23.
Weedman, D. W. 1977, *Ann. Rev. Astr. Ap.*, **15**, 69.
Wirth, A., Kenyon, S. J., and Hunter, D. A. 1983, *Ap. J.*, **269**, 102.
Wrobel, J. M. 1984, *Ap. J.*, **284**, 531.
Wrobel, J. M., Jones, D. J., and Shaffer, D. B. 1985, *Ap. J.*, **289**, 598.
Young, P. J. 1976, *A.J.*, **81**, 807.

DONG-WOO KIM: Harvard-Smithsonian Center for Astrophysics, 60 Garden Street, Cambridge, MA 02145